



Measurement of the semileptonic b branching fractions and average b mixing parameter in Z decays

P. Abreu, W. Adam, T. Adye, P. Adzic, I. Ajinenko, Z. Albrecht, T. Alderweireld, G D. Alekseev, R. Alemany, T. Allmendinger, et al.

► To cite this version:

P. Abreu, W. Adam, T. Adye, P. Adzic, I. Ajinenko, et al.. Measurement of the semileptonic b branching fractions and average b mixing parameter in Z decays. European Physical Journal C: Particles and Fields, 2001, 20, pp.455-478. 10.1007/s100520100690 . in2p3-00010185

HAL Id: in2p3-00010185

<https://hal.in2p3.fr/in2p3-00010185>

Submitted on 1 Aug 2001

HAL is a multi-disciplinary open access archive for the deposit and dissemination of scientific research documents, whether they are published or not. The documents may come from teaching and research institutions in France or abroad, or from public or private research centers.

L'archive ouverte pluridisciplinaire **HAL**, est destinée au dépôt et à la diffusion de documents scientifiques de niveau recherche, publiés ou non, émanant des établissements d'enseignement et de recherche français ou étrangers, des laboratoires publics ou privés.

Measurement of the semileptonic b branching fractions and average b mixing parameter in Z decays

DELPHI Collaboration

Abstract

The semileptonic branching fractions for primary and cascade b decays $\text{BR}(b \rightarrow \ell^-)$, $\text{BR}(b \rightarrow c \rightarrow \ell^+)$ and $\text{BR}(b \rightarrow \bar{c} \rightarrow \ell^-)$ were measured in hadronic Z decays collected by the DELPHI experiment at LEP.

The sample was enriched in b decays using the lifetime information and various techniques were used to separate leptons from direct or cascade b decays.

By fitting the momentum spectra of di-leptons in opposite jets, the average b mixing parameter $\bar{\chi}$ was also extracted.

The following results have been obtained:

$$\begin{aligned} \text{BR}(b \rightarrow \ell^-) &= (10.70 \pm 0.08(\text{stat}) \pm 0.21(\text{syst})_{+0.44}^{-0.30}(\text{model}))\% \\ \text{BR}(b \rightarrow c \rightarrow \ell^+) &= (7.98 \pm 0.22(\text{stat}) \pm 0.21(\text{syst})_{-0.20}^{+0.14}(\text{model}))\% \\ \text{BR}(b \rightarrow \bar{c} \rightarrow \ell^-) &= (1.61 \pm 0.20(\text{stat}) \pm 0.17(\text{syst})_{-0.44}^{+0.30}(\text{model}))\% \\ \bar{\chi} &= 0.127 \pm 0.013(\text{stat}) \pm 0.005(\text{syst}) \pm 0.004(\text{model}) \end{aligned}$$

(Accepted by Eur.Phys.J.C)

P.Abreu²¹, W.Adam⁵¹, T.Adye³⁷, P.Adzic¹², I.Ajinenko⁴³, Z.Albrecht¹⁸, T.Alderweireld², G.D.Alekseev¹⁷, R.Aleman⁵⁰, T.Allmendinger¹⁸, P.P.Allport²², S.Almehed²⁴, U.Amaldi²⁸, N.Amapane⁴⁶, S.Amato⁴⁸, E.G.Anassontzis³, P.Andersson⁴⁵, A.AndreaZZa²⁷, S.Andringa²¹, P.Antilogus²⁵, W-D.Apel¹⁸, Y.Arnoud¹⁵, B.Åsman⁴⁵, J-E.Augustin²³, A.Augustinus⁹, P.Baillon⁹, A.Ballestrero⁴⁶, P.Bambade^{9,20}, F.Barao²¹, G.Barbiellini⁴⁷, R.Barbier²⁵, D.Y.Bardin¹⁷, G.Barker¹⁸, A.Baroncelli³⁹, M.Battaglia¹⁶, M.Baubillier²³, K-H.Becks⁵³, M.Begalli⁶, A.Behrmann⁵³, P.Beilliere⁸, Yu.Belokopytov⁹, N.C.Benekos³², A.C.Benvenuti⁵, C.Berat¹⁵, M.Berggren²³, L.Berntzon⁴⁵, D.Bertrand², M.Besancon⁴⁰, M.S.Bilenky¹⁷, M-A.Bizouard²⁰, D.Bloch¹⁰, H.M.Blom³¹, M.Bonesini²⁸, M.Boonekamp⁴⁰, P.S.L.Booth²², G.Borisov²⁰, C.Bosio⁴², O.Botner⁴⁹, E.Boudinov³¹, B.Bouquet²⁰, C.Bourdarios²⁰, T.J.V.Bowcock²², I.Boyko¹⁷, I.Bozovic¹², M.Bozzo¹⁴, M.Bracko⁴⁴, P.Branchini³⁹, R.A.Brenner⁴⁹, P.Bruckman⁹, J-M.Brunet⁸, L.Bugge³³, T.Buran³³, B.Buschbeck⁵¹, P.Buschmann⁵³, S.Cabrera⁵⁰, M.Caccia²⁷, M.Calvi²⁸, T.Camporesi⁹, V.Canale³⁸, F.Carena⁹, L.Carroll²², C.Caso¹⁴, M.V.Castillo Gimenez⁵⁰, A.Cattai⁹, F.R.Cavallo⁵, Ph.Charpentier⁹, P.Checchia³⁶, G.A.Chelkov¹⁷, R.Chierici⁴⁶, P.Chliapnikov^{9,43}, P.Chochula⁷, V.Chorowicz²⁵, J.Chudoba³⁰, K.Cieslik¹⁹, P.Collins⁹, R.Contri¹⁴, E.Cortina⁵⁰, G.Cosme²⁰, F.Cossutti⁹, M.Costa⁵⁰, H.B.Crawley¹, D.Crennell³⁷, G.Crosetti¹⁴, J.Cuevas Maestro³⁴, S.Czellar¹⁶, J.D'Hondt², J.Dalmau⁴⁵, M.Davenport⁹, W.Da Silva²³, G.Della Ricca⁴⁷, P.Delpierre²⁶, N.Demaria⁴⁶, A.De Angelis⁴⁷, W.De Boer¹⁸, C.De Clercq², B.De Lotto⁴⁷, A.De Min⁹, L.De Paula⁴⁸, H.Dijkstra⁹, L.Di Ciaccio³⁸, J.Dolbeau⁸, K.Doroba⁵², M.Dracos¹⁰, J.Drees⁵³, M.Dris³², G.Eigen⁴, T.Ekelof⁴⁹, M.Ellert⁴⁹, M.Elsing⁹, J-P.Engel¹⁰, M.Espírito Santo⁹, G.Fanourakis¹², D.Fassouliotis¹², M.Feindt¹⁸, J.Fernandez⁴¹, A.Ferre⁵⁰, E.Ferrer-Ribas²⁰, F.Ferro¹⁴, A.Firestone¹, U.Flagmeyer⁵³, H.Foeth⁹, E.Fokitis³², F.Fontanelli¹⁴, B.Franek³⁷, A.G.Frodesen⁴, R.Fruhwirth⁵¹, F.Fulda-Quenzer²⁰, J.Fuster⁵⁰, A.Galloni²², D.Gamba⁴⁶, S.Gamblin²⁰, M.Gandelman⁴⁸, C.Garcia⁵⁰, C.Gaspar⁹, M.Gaspar⁴⁸, U.Gasparini³⁶, Ph.Gavillet⁹, E.N.Gazis³², D.Gele¹⁰, T.Geralis¹², L.Gerdyukov⁴³, N.Ghodbane²⁵, I.Gil⁵⁰, F.Glege⁵³, R.Gokieli^{9,52}, B.Golob^{9,44}, G.Gomez-Ceballos⁴¹, P.Goncalves²¹, I.Gonzalez Caballero⁴¹, G.Gopal³⁷, L.Gorn¹, Yu.Gouz⁴³, V.Gracco¹⁴, J.Grahl¹, E.Graziani³⁹, P.Gris⁴⁰, G.Grosdidier²⁰, K.Grzelak⁵², J.Guy³⁷, C.Haag¹⁸, F.Hahn⁹, S.Hahn⁵³, S.Haider⁹, A.Hallgren⁴⁹, K.Hamacher⁵³, J.Hansen³³, F.J.Harris³⁵, F.Hauler¹⁸, V.Hedberg^{9,24}, S.Heising¹⁸, J.J.Hernandez⁵⁰, P.Herquet², H.Herr⁹, E.Higon⁵⁰, S-O.Holmgren⁴⁵, P.J.Holt³⁵, S.Hoorelbeke², M.Houlden²², J.Hrubic⁵¹, M.Huber¹⁸, G.J.Hughes²², K.Hultqvist^{9,45}, J.N.Jackson²², R.Jacobsson⁹, P.Jalocha¹⁹, R.Janik⁷, Ch.Jarlskog²⁴, G.Jarlskog²⁴, P.Jarry⁴⁰, B.Jean-Marie²⁰, D.Jeans³⁵, E.K.Johansson⁴⁵, P.Jonsson²⁵, C.Joram⁹, P.Juillot¹⁰, L.Jungermann¹⁸, F.Kapusta²³, K.Karafasoulis¹², S.Katsanevas²⁵, E.C.Katsoufis³², R.Keranen¹⁸, G.Kernel⁴⁴, B.P.Kersevan⁴⁴, Yu.Khokhlov⁴³, B.A.Khomenko¹⁷, N.N.Khovanski¹⁷, A.Kiiskinen¹⁶, B.King²², A.Kinvig²², N.J.Kjaer⁹, O.Klapp⁵³, P.Kluit³¹, P.Kokkinias¹², V.Kostioukhine⁴³, C.Kourkoumelis³, O.Kouznetsov¹⁷, M.Krammer⁵¹, E.Kriznic⁴⁴, Z.Krumstein¹⁷, P.Kubinec⁷, J.Kurowska⁵², K.Kurvinen¹⁶, J.W.Lamsa¹, D.W.Lane¹, J-P.Laugier⁴⁰, R.Lauhakangas¹⁶, G.Leder⁵¹, F.Ledroit¹⁵, L.Leinonen⁴⁵, A.Leisos¹², R.Leitner³⁰, G.Lenzen⁵³, V.Lepeltier²⁰, T.Lesiak¹⁹, M.Lethuillier²⁵, J.Libby³⁵, W.Liebig⁵³, D.Liko⁹, A.Lipniacka⁴⁵, I.Lippi³⁶, B.Loerstad²⁴, J.G.Loken³⁵, J.H.Lopes⁴⁸, J.M.Lopez⁴¹, R.Lopez-Fernandez¹⁵, D.Loukas¹², P.Lutz⁴⁰, L.Lyons³⁵, J.MacNaughton⁵¹, J.R.Mahon⁶, A.Maio²¹, A.Malek⁵³, S.Maltezos³², V.Malychev¹⁷, F.Mandl⁵¹, J.Marco⁴¹, R.Marco⁴¹, B.Marechal⁴⁸, M.Margoni³⁶, J-C.Marin⁹, C.Mariotti⁹, A.Markou¹², C.Martinez-Rivero⁹, S.Marti i Garcia⁹, J.Masik¹³, N.Mastroiannopoulos¹², F.Matorras⁴¹, C.Matteuzzi²⁸, G.Matthiae³⁸, F.Mazzucato³⁶, M.Mazzucato³⁶, M.Mc Cubbin²², R.Mc Kay¹, R.Mc Nulty²², G.Mc Pherson²², E.Merle¹⁵, C.Meroni²⁷, W.T.Meyer¹, E.Migliore⁹, L.Mirabito²⁵, W.A.Mitaroff⁵¹, U.Mjoernmark²⁴, T.Moa⁴⁵, M.Moch¹⁸, R.Moeller²⁹, K.Moenig^{9,11}, M.R.Monge¹⁴, D.Moraes⁴⁸, P.Morettini¹⁴, G.Morton³⁵, U.Mueller⁵³, K.Muenich⁵³, M.Mulders³¹, C.Mulet-Marquis¹⁵, L.M.Mundim⁶, R.Muresan²⁴, W.J.Murray³⁷, B.Muryn¹⁹, G.Myatt³⁵, T.Myklebust³³, F.Naraghi¹⁵, M.Nassiakou¹², F.L.Navarria⁵, K.Nawrocki⁵², P.Negri²⁸, N.Neufeld⁵¹, R.Nicolaidou⁴⁰, B.S.Nielsen²⁹, P.Niezurawski⁵², M.Nikolenko^{10,17}, V.Nomokonov¹⁶, A.Nygren²⁴, V.Obraztsov⁴³, A.G.Olshevski¹⁷, A.Onofre²¹, R.Orava¹⁶, G.Orazi¹⁰, K.Osterberg⁹, A.Ouraou⁴⁰, A.Oyanguren⁵⁰, M.Paganoni²⁸, S.Paiano⁵, R.Pain²³, R.Paiva²¹, J.Palacios³⁵, H.Palka¹⁹, Th.D.Papadopoulou³², L.Pape⁹, C.Parkes⁹, F.Parodi¹⁴, U.Parzefall²², A.Passeri³⁹, O.Passon⁵³, T.Pavel²⁴, M.Pegoraro³⁶, L.Peralta²¹, M.Pernicka⁵¹, A.Perrotta⁵, C.Petridou⁴⁷, A.Petrolini¹⁴, H.T.Phillips³⁷, F.Pierre⁴⁰, M.Pimenta²¹, E.Piotto²⁷, T.Podobnik⁴⁴, V.Poireau⁴⁰, M.E.Pol⁶, G.Polok¹⁹, P.Poropat⁴⁷, V.Pozdniakov¹⁷, P.Privitera³⁸, N.Pukhaeva¹⁷, A.Pullia²⁸, D.Radojicic³⁵, S.Ragazzi²⁸, H.Rahmani³², J.Rames¹³, A.L.Read³³, P.Rebecchi⁹, N.G.Redaeli²⁸, M.Regler⁵¹, J.Rehn¹⁸, D.Reid³¹, P.Reinertsen⁴, R.Reinhardt⁵³, P.B.Renton³⁵, L.K.Resvanis³, F.Richard²⁰, J.Ridky¹³, G.Rinaudo⁴⁶, I.Ripp-Baudot¹⁰, A.Romero⁴⁶, P.Ronchese³⁶, E.I.Rosenberg¹, P.Rosinsky⁷, P.Roudeau²⁰, T.Rovelli⁵, V.Ruhlmann-Kleider⁴⁰, A.Ruiz⁴¹, H.Saarikko¹⁶, Y.Sacquin⁴⁰, A.Sadovsky¹⁷, G.Sajot¹⁵, J.Salt⁵⁰, D.Sampsonidis¹², M.Sannino¹⁴, A.Savoy-Navarro²³, Ph.Schwemling²³, B.Schwering⁵³, U.Schwickerath¹⁸, F.Scuri⁴⁷, Y.Sedykh¹⁷, A.M.Segar³⁵, N.Seibert¹⁸, R.Sekulin³⁷, G.Sette¹⁴, R.C.Shellard⁶, M.Siebel⁵³, L.Simard⁴⁰, F.Simonetto³⁶, A.N.Sisakian¹⁷, G.Smadja²⁵, N.Smirnov⁴³, O.Smirnova²⁴, G.R.Smith³⁷, A.Sokolov⁴³, A.Sopczak¹⁸, R.Sosnowski⁵², T.Spaso⁹, E.Spiriti³⁹, S.Squarcia¹⁴, C.Stanescu³⁹, M.Stanitzki¹⁸, K.Stevenson³⁵, A.Stocchi²⁰, J.Strauss⁵¹, R.Strub¹⁰, B.Stugu⁴, M.Szczekowski⁵², M.Szeptycka⁵², T.Tabarelli²⁸, A.Taffard²², O.Tchikilev⁴³, F.Tegenfeldt⁴⁹, F.Terranova²⁸, J.Timmermans³¹, N.Tinti⁵, L.G.Tkatchev¹⁷, M.Tobin²², S.Todorova⁹, B.Tome²¹, A.Tonazzo⁹, L.Tortora³⁹, P.Tortosa⁵⁰, G.Transtomer²⁴, D.Treille⁹, G.Tristram⁸, M.Trochimczuk⁵², C.Troncon²⁷, M-L.Turluer⁴⁰, I.A.Tyapkin¹⁷, P.Tyapkin²⁴, S.Tzamaras¹², O.Ullaland⁹, V.Uvarov⁴³, G.Valenti^{9,5}, E.Vallazza⁴⁷, P.Van Dam³¹, W.Van den Boeck², W.K.Van Doninck², J.Van Eldik^{9,31}, A.Van Lysebetten²,

N.van Remortel², I.Van Vulpen³¹, G.Vegni²⁷, L.Ventura³⁶, W.Venus^{37,9}, F.Verbeure², P.Verdier²⁵, M.Verlato³⁶, L.S.Vertogradov¹⁷, V.Verzi²⁷, D.Vilanova⁴⁰, L.Vitale⁴⁷, E.Vlasov⁴³, A.S.Vodopyanov¹⁷, G.Voulgaris³, V.Vrba¹³, H.Wahlen⁵³, A.J.Washbrook²², C.Weiser⁹, D.Wicke⁹, J.H.Wickens², G.R.Wilkinson³⁵, M.Winter¹⁰, M.Witek¹⁹, G.Wolf⁹, J.Yi¹, O.Yushchenko⁴³, A.Zalewska¹⁹, P.Zalewski⁵², D.Zavrtanik⁴⁴, E.Zevgolatakos¹², N.I.Zimin^{17,24}, A.Zintchenko¹⁷, Ph.Zoller¹⁰, G.Zumerle³⁶, M.Zupan¹²

¹Department of Physics and Astronomy, Iowa State University, Ames IA 50011-3160, USA

²Physics Department, Univ. Instelling Antwerpen, Universiteitsplein 1, B-2610 Antwerpen, Belgium
and IIHE, ULB-VUB, Pleinlaan 2, B-1050 Brussels, Belgium

and Faculté des Sciences, Univ. de l'Etat Mons, Av. Maistriau 19, B-7000 Mons, Belgium

³Physics Laboratory, University of Athens, Solonos Str. 104, GR-10680 Athens, Greece

⁴Department of Physics, University of Bergen, Allégaten 55, NO-5007 Bergen, Norway

⁵Dipartimento di Fisica, Università di Bologna and INFN, Via Imerio 46, IT-40126 Bologna, Italy

⁶Centro Brasileiro de Pesquisas Físicas, rua Xavier Sigaud 150, BR-22290 Rio de Janeiro, Brazil

and Depto. de Física, Pont. Univ. Católica, C.P. 38071 BR-22453 Rio de Janeiro, Brazil

and Inst. de Física, Univ. Estadual do Rio de Janeiro, rua São Francisco Xavier 524, Rio de Janeiro, Brazil

⁷Comenius University, Faculty of Mathematics and Physics, Mlynska Dolina, SK-84215 Bratislava, Slovakia

⁸Collège de France, Lab. de Physique Corpusculaire, IN2P3-CNRS, FR-75231 Paris Cedex 05, France

⁹CERN, CH-1211 Geneva 23, Switzerland

¹⁰Institut de Recherches Subatomiques, IN2P3 - CNRS/ULP - BP20, FR-67037 Strasbourg Cedex, France

¹¹Now at DESY-Zeuthen, Platanenallee 6, D-15735 Zeuthen, Germany

¹²Institute of Nuclear Physics, N.C.S.R. Demokritos, P.O. Box 60228, GR-15310 Athens, Greece

¹³FZU, Inst. of Phys. of the C.A.S. High Energy Physics Division, Na Slovance 2, CZ-180 40, Praha 8, Czech Republic

¹⁴Dipartimento di Fisica, Università di Genova and INFN, Via Dodecaneso 33, IT-16146 Genova, Italy

¹⁵Institut des Sciences Nucléaires, IN2P3-CNRS, Université de Grenoble 1, FR-38026 Grenoble Cedex, France

¹⁶Helsinki Institute of Physics, HIP, P.O. Box 9, FI-00014 Helsinki, Finland

¹⁷Joint Institute for Nuclear Research, Dubna, Head Post Office, P.O. Box 79, RU-101 000 Moscow, Russian Federation

¹⁸Institut für Experimentelle Kernphysik, Universität Karlsruhe, Postfach 6980, DE-76128 Karlsruhe, Germany

¹⁹Institute of Nuclear Physics and University of Mining and Metallurgy, Ul. Kawiora 26a, PL-30055 Krakow, Poland

²⁰Université de Paris-Sud, Lab. de l'Accélérateur Linéaire, IN2P3-CNRS, Bât. 200, FR-91405 Orsay Cedex, France

²¹LIP, IST, FCUL - Av. Elias Garcia, 14-1º, PT-1000 Lisboa Codex, Portugal

²²Department of Physics, University of Liverpool, P.O. Box 147, Liverpool L69 3BX, UK

²³LPNHE, IN2P3-CNRS, Univ. Paris VI et VII, Tour 33 (RdC), 4 place Jussieu, FR-75252 Paris Cedex 05, France

²⁴Department of Physics, University of Lund, Sölvegatan 14, SE-223 63 Lund, Sweden

²⁵Université Claude Bernard de Lyon, IPNL, IN2P3-CNRS, FR-69622 Villeurbanne Cedex, France

²⁶Univ. d'Aix - Marseille II - CPP, IN2P3-CNRS, FR-13288 Marseille Cedex 09, France

²⁷Dipartimento di Fisica, Università di Milano and INFN-MILANO, Via Celoria 16, IT-20133 Milan, Italy

²⁸Dipartimento di Fisica, Univ. di Milano-Bicocca and INFN-MILANO, Piazza della Scienza 3, IT-20126 Milan, Italy

²⁹Niels Bohr Institute, Blegdamsvej 17, DK-2100 Copenhagen Ø, Denmark

³⁰IPNP of MFF, Charles Univ., Areal MFF, V Holesovickach 2, CZ-180 00, Praha 8, Czech Republic

³¹NIKHEF, Postbus 41882, NL-1009 DB Amsterdam, The Netherlands

³²National Technical University, Physics Department, Zografou Campus, GR-15773 Athens, Greece

³³Physics Department, University of Oslo, Blindern, NO-1000 Oslo 3, Norway

³⁴Dpto. Física, Univ. Oviedo, Avda. Calvo Sotelo s/n, ES-33007 Oviedo, Spain

³⁵Department of Physics, University of Oxford, Keble Road, Oxford OX1 3RH, UK

³⁶Dipartimento di Fisica, Università di Padova and INFN, Via Marzolo 8, IT-35131 Padua, Italy

³⁷Rutherford Appleton Laboratory, Chilton, Didcot OX11 0QX, UK

³⁸Dipartimento di Fisica, Università di Roma II and INFN, Tor Vergata, IT-00173 Rome, Italy

³⁹Dipartimento di Fisica, Università di Roma III and INFN, Via della Vasca Navale 84, IT-00146 Rome, Italy

⁴⁰DAPNIA/Service de Physique des Particules, CEA-Saclay, FR-91191 Gif-sur-Yvette Cedex, France

⁴¹Instituto de Física de Cantabria (CSIC-UC), Avda. los Castros s/n, ES-39006 Santander, Spain

⁴²Dipartimento di Fisica, Università degli Studi di Roma La Sapienza, Piazzale Aldo Moro 2, IT-00185 Rome, Italy

⁴³Inst. for High Energy Physics, Serpukov P.O. Box 35, Protvino, (Moscow Region), Russian Federation

⁴⁴J. Stefan Institute, Jamova 39, SI-1000 Ljubljana, Slovenia and Laboratory for Astroparticle Physics,

Nova Gorica Polytechnic, Kostanjevska 16a, SI-5000 Nova Gorica, Slovenia,

and Department of Physics, University of Ljubljana, SI-1000 Ljubljana, Slovenia

⁴⁵Fysikum, Stockholm University, Box 6730, SE-113 85 Stockholm, Sweden

⁴⁶Dipartimento di Fisica Sperimentale, Università di Torino and INFN, Via P. Giuria 1, IT-10125 Turin, Italy

⁴⁷Dipartimento di Fisica, Università di Trieste and INFN, Via A. Valerio 2, IT-34127 Trieste, Italy

and Istituto di Fisica, Università di Udine, IT-33100 Udine, Italy

⁴⁸Univ. Federal do Rio de Janeiro, C.P. 68528 Cidade Univ., Ilha do Fundão BR-21945-970 Rio de Janeiro, Brazil

⁴⁹Department of Radiation Sciences, University of Uppsala, P.O. Box 535, SE-751 21 Uppsala, Sweden

⁵⁰IFIC, Valencia-CSIC, and D.F.A.M.N., U. de Valencia, Avda. Dr. Moliner 50, ES-46100 Burjassot (Valencia), Spain

⁵¹Institut für Hochenergiephysik, Österr. Akad. d. Wissensch., Nikolsdorfergasse 18, AT-1050 Vienna, Austria

⁵²Inst. Nuclear Studies and University of Warsaw, Ul. Hoza 69, PL-00681 Warsaw, Poland

⁵³Fachbereich Physik, University of Wuppertal, Postfach 100 127, DE-42097 Wuppertal, Germany

1 Introduction

Measurements of the direct semileptonic branching fractions of b -hadrons are important in order to understand the dynamics of heavy quark decays and to determine the weak couplings of quarks to the W boson. From a precise measurement of the inclusive semileptonic branching fractions of b quarks a precise value of the Cabibbo-Kobayashi-Maskawa matrix element $|V_{cb}|$ can be calculated [1].

These measurements have been performed both at the $\Upsilon(4S)$ and in hadronic Z decays. In order to make a comparison between the two sets of results, the fact that the composition of the inclusive sample is different in the two cases must be taken into account. At low energy only B^- and \bar{B}^0 mesons are produced, while at the Z , \bar{B}_s^0 mesons and b -baryons are also present. Assuming the semileptonic widths of all b -hadrons to be equal, their respective semileptonic branching fractions are expected to be proportional to their measured lifetimes. The ratio between the B^- and \bar{B}^0 lifetimes to the inclusive b -hadron lifetime measured at the Z , is at present larger than 1, whereas the semileptonic branching fractions of b -hadrons measured at the Z are slightly larger than the ones measured at the $\Upsilon(4S)$ [2],[3].

Theoretical calculations which include higher order perturbative QCD corrections give a prediction of the branching fraction value correlated with the prediction for $\langle n_c \rangle$, the average number of charmed hadrons produced per b -hadron decay [4]. These results are compatible with the present LEP measurements.

In this paper, the two cascade processes: $b \rightarrow c \rightarrow \ell^+$ and $b \rightarrow \bar{c} \rightarrow \ell^-$ are also considered, not only because they are the main source of background to the direct decays, but also because the values of these branching fractions are important inputs to several other heavy flavour measurements, like asymmetries and oscillations measurements. The $\text{BR}(b \rightarrow \bar{c} \rightarrow \ell^-)$ measurement presented in this paper is the first inclusive measurement of “right sign” leptons from cascade decays of b -hadrons.

In addition, the average $B^0 - \bar{B}^0$ mixing parameter is measured. It is the time integrated probability that a b -hadron oscillates into a \bar{b} -hadron: $\bar{\chi} = \frac{b \rightarrow \bar{B}^0 \rightarrow B^0 \rightarrow \ell^+ X}{b \rightarrow \ell^\pm X}$. It is related to the mixing parameters of B_d^0 and B_s^0 mesons, χ_d and χ_s respectively, by: $\bar{\chi} = g_{B_d^0} \chi_d + g_{B_s^0} \chi_s$, where $g_{B_d^0}$ and $g_{B_s^0}$ are the production fractions of B_d^0 and B_s^0 in semileptonic decays. Its measurement can therefore be used in the evaluation of the production fraction of B_s^0 mesons [1].

This paper presents the measurement of inclusive semileptonic branching fractions of b quarks in hadronic Z decays using data collected with the DELPHI detector at LEP. Four analyses have been performed, using different strategies and using various data samples, partially overlapping. Events containing b hadrons were selected using lifetime information, electrons and muons were identified and several different techniques were used to determine the origin of the lepton. Direct and cascade branching fractions: $\text{BR}(b \rightarrow \ell^-)$, $\text{BR}(b \rightarrow c \rightarrow \ell^+)$ and $\text{BR}(b \rightarrow \bar{c} \rightarrow \ell^-)$ were measured and, by fitting the momentum spectra of di-leptons in opposite jets, the average $B^0 - \bar{B}^0$ mixing parameter $\bar{\chi}$ was also extracted.

The previous DELPHI results on the semileptonic branching fractions [5] were obtained with data collected at LEP in 1991 and 1992, using electrons and muons in a sample of hadronic Z decays, with natural composition of quark flavours. A global fit to several electroweak parameters was performed. With respect to that analysis there is little dependence on the partial decay widths of the Z into $b\bar{b}$ and $c\bar{c}$ quark pairs ($R_b = \Gamma_{b\bar{b}}/\Gamma_{had}$, $R_c = \Gamma_{c\bar{c}}/\Gamma_{had}$) and the background due to misidentified hadrons and leptons from decays and punch-through of light hadrons has been reduced. The present result supersedes the previous result obtained by DELPHI [5].

The layout of the paper is the following: a description of the DELPHI detector is given in Section 2. The selection of the hadronic event sample is described in Section 3. The b -flavour tagging algorithm is described in Section 4. A brief summary of the performances of lepton identification algorithms is given in Section 5. Results obtained in the different analyses are then described in the following Sections: single and di-lepton analysis (Section 6), single lepton and jet-charge analysis (Section 7), multitag analysis (Section 8) and inclusive b -hadron reconstruction analysis (Section 9). Finally, in Section 10 averages of the results obtained in the different analyses are calculated.

2 The DELPHI detector

The DELPHI detector has been described in detail in reference [6]. Only the components relevant to this analysis are mentioned here.

In the barrel region, the charged particles are measured by a set of cylindrical tracking detectors with a common axis parallel to the 1.2 T solenoidal magnetic field and to the beam direction. The time projection chamber (TPC) is the main tracking device. The TPC is a cylinder with a length of 3 m, an inner radius of 30 cm and an outer radius of 122 cm. Tracks are reconstructed using up to 16 space points in the region $39^\circ < \theta < 141^\circ$, where θ is the polar angle with respect to the beam direction. Tracks can be reconstructed using at least 4 space points down to 21° and 159° .

Additional precise $R\Phi$ measurements, in the plane perpendicular to the magnetic field, are provided at larger and smaller radii by the Outer and Inner detectors, respectively. The Outer Detector (OD) has five layers of drift cells at radii between 198 and 206 cm and covers polar angles from 42° to 138° . The Inner Detector (ID) is a cylindrical drift chamber having inner radius of 12 cm and outer radius of 28 cm and covers polar angles from 23° to 157° . It contains a jet chamber section providing 24 $R\Phi$ coordinates measurements surrounded by five layers of proportional chambers with both $R\Phi$ and longitudinal z coordinates measurements.

The micro-vertex detector (VD) [7] is located between the LEP beam pipe and the ID. It consists of three concentric layers of silicon micro-vertex detectors placed at radii of 6.3, 9.0 and 10.9 cm from the interaction region, called closer, inner and outer layer, respectively. For all layers the micro-vertex detectors provide hits in the $R\Phi$ -plane with a measured intrinsic resolution of about $8\ \mu\text{m}$; the inner and outer layers provide in addition measurements in the z direction, with a precision depending on the polar angle and reaching a value of $9\ \mu\text{m}$ for tracks perpendicular to the modules. The polar angle coverage for charged particles hitting all three layers of the detector is $44^\circ < \theta < 136^\circ$; the closer layer coverage goes down to 25° . The z measurement was only available in 1994 and 1995.

Additional information for particle identification is provided by the Ring Imaging Cherenkov counters (RICH) measuring the Cherenkov light emitted by particles traversing a dielectric medium faster than the speed of light. The barrel part of the detector covers polar angles from 40° to 140° . To cover a large momentum range, a liquid (C_6F_{14}) and a gas (C_5F_{12}) radiator are used.

The barrel electromagnetic calorimeter, HPC, covers the polar angles between 42° and 138° . It is a gas-sampling device which provides complete three dimensional charge information in the same way as a time projection chamber. Each shower is sampled nine times in its longitudinal development. Along the drift direction, parallel to the DELPHI magnetic field, the shower is sampled every 3.5 mm ; in the plane perpendicular to the

drift the charge is collected by cathode pads of variable size, ranging from 2.3 cm in the inner part of the detector to 7 cm in the outer layers.

In the forward regions the tracking is completed by two sets of planar drift chambers (FCA and FCB) placed at distances of ± 165 cm and ± 275 cm from the interaction point. A lead glass calorimeter (EMF) is used to reconstruct electromagnetic energy in the forward region.

For the identification of hadronic showers, the iron return yoke of the magnet is instrumented with limited streamer mode detectors to create a sampling gas calorimeter, the Hadronic Calorimeter (HAC).

Muon identification in the barrel region is based on a set of muon chambers (MUB), covering polar angles between 53° and 127° . It consists of six active planes of drift chambers, two inside the return yoke of the magnet after 90 cm of iron (inner layer) and four outside after a further 20 cm of iron (outer and peripheral layers). The inner and outer modules have similar azimuthal coverage. The gaps in azimuth between adjacent modules are covered by the peripheral modules. Therefore a muon traverses typically either two inner layer chambers and two outer layer chambers, or just two peripheral layer chambers. Each chamber measures the $R\Phi$ coordinate with a precision of about 2-3 mm. Measuring $R\Phi$ in both the inner layer and the outer or peripheral layer determines the azimuthal angle of muon candidates leaving the return yoke within about $\pm 1^\circ$. These errors are much smaller than the effects of multiple scattering on muons traversing the iron.

In the forward region the muon identification is done using two sets of planar drift chambers (MUF) covering the angular region between 11° and 45° . The first set is placed behind 85 cm of iron and the second one behind an additional 20 cm. Each set consists of two orthogonal layers of drift chambers where the anode is read out directly and the cathode via a delay line to measure the coordinate along the wire. The resolution in both coordinates is about 4 mm.

3 Event selection

Charged particles were accepted if their polar angle was between 20° and 160° , their track length was larger than 30 cm, their impact parameter relative to the interaction point was less than 5 cm in the plane perpendicular to the beam direction and less than 10 cm along the beam direction and their momentum was larger than 200 MeV/ c with a relative error smaller than 100%. Neutral particles detected in the HPC and EMF or in the hadronic calorimeters were required to have a measured energy larger than 500 MeV.

The decays of the Z to hadrons were selected by requiring a total energy of the charged particles (assumed to be pions) larger than 15% of the center-of-mass energy and at least 7 reconstructed charged particles. With these criteria, the efficiency to select $q\bar{q}$ events from the simulation was about 95%. All sources of background have been found to be below 0.1%. No significant differences in the acceptance between different flavours have been found.

For each event the thrust axis was calculated from the selected charged and neutral particles. Only events with: $|\cos\theta_{thrust}| < 0.90$ were used. Requiring, in addition, that all sub-detectors needed for these analyses were fully operating, totals of about 1 030 000 and 515 000 Z hadronic decays were selected from the 1994 and 1995 data samples, respectively. About 3 800 000 events were selected from a simulated sample of $Z \rightarrow q\bar{q}$ events. A reduced angular region was used in some parts of the following analyses to ensure an efficient acceptance for the vertex detector.

Events were generated with the JETSET 7.3 generator [8] using parton shower and string fragmentation with parameters optimized to describe the hadronic distributions as measured by DELPHI [9]. Generated events were passed through a detailed simulation [6] which modeled the detector response and processed through the same analysis chain as the real data. Jets were formed from the charged and neutral particles using the JADE algorithm with $Y_{cut}^{min} = 0.02$ [10]. The transverse momentum of the lepton (p_t) was determined relative to the direction of the jet, excluding the lepton itself.

Any differences with respect to these selection criteria, as well as their effect on the statistics used, will be explicitly described for each analysis. The four analyses used different data subsamples corresponding to the optimal operation of the subdetectors relevant to the definition of the variables used. Analysis I and IV used 1994 and 1995 data samples, Analysis III used also 1992 and 1993 data, while Analysis II used 1994 only. The 1992 and 1993 statistics are given in Section 8.

4 b -flavour tagging

A b -flavour tagging algorithm was used in order to obtain a sample enriched in $Z \rightarrow b\bar{b}$ events. Events were divided into two hemispheres, with respect to a plane perpendicular to the thrust axis and passing through the beam interaction point. The b -flavour tagging algorithm was applied separately to each hemisphere. Analyses I and IV used the combined b -flavour tagging algorithm described in [11]. This algorithm combines, in a single variable, several quantities which are sensitive to the presence of a b -hadron.

The main discriminant variable is the probability for all tracks belonging to the hemisphere to come from the primary vertex, calculated from the impact parameters of the tracks positively signed according to the lifetime convention. Other variables were defined for hemispheres containing a secondary vertex. These variables are: the effective mass of the system of particles attached to the secondary vertex, the rapidity of these tracks with respect to the jet direction and the fraction of the charged energy of the jet which is included in the secondary vertex. Optimized levels of efficiency and purity were chosen in each analysis.

Analysis II used a b -flavour tagging algorithm exploiting only the information from the impact parameters of charged particles [11]. Analysis III used a multivariate method to tag the flavours, as described in Section 8.1.

5 Lepton sample

5.1 Muon identification

To identify a charged particle with momentum greater than 3 GeV/ c as a muon candidate, its track was extrapolated to each of the layers of the muon chambers taking into account multiple scattering in the material and the propagation of track reconstruction errors. A fit was then made between the track extrapolation and the position and direction of the hits in the muon chambers. Ambiguities with muon chamber hits associated to more than one extrapolated track were resolved by selecting the track with the best fit. The charged particle was then identified as a muon if the fit was sufficiently good and if hits were found outside the return iron yoke.

To exclude regions with poor geometrical acceptance, a muon was accepted only if its polar angle, θ_μ , was within one of the following intervals:

$$0.03 < |\cos \theta_\mu| < 0.62 \quad \text{or} \quad 0.68 < |\cos \theta_\mu| < 0.95,$$

which defined the barrel and the forward regions, respectively.

The muon identification efficiency was measured in $Z \rightarrow \mu^+\mu^-$ events, in the decays of taus into muons and using muons from two-photon collisions $\gamma\gamma \rightarrow \mu^+\mu^-$. A mean efficiency of 0.82 ± 0.01 was found with little dependence on the muon momentum and on the track polar angle. Predictions of the simulation agree with corresponding measurements in data, both in absolute value and in the momentum dependence, within a precision of 1.5%.

An estimate of the misidentification probability was obtained by means of a lifetime-based anti b -tag to select a background enriched sample. After the subtraction of the muon content in the selected sample, the misidentification probability was found to be $(0.52 \pm 0.03)\%$ in the barrel and $(0.36 \pm 0.06)\%$ in the forward regions. Applying the same procedure to the simulation gave however lower values, with factors 2.03 ± 0.12 (2.02 ± 0.13) in the barrel and 1.22 ± 0.20 (1.78 ± 0.24) in the forward regions for the 1994 (1995) samples, respectively, showing a small momentum dependence and about 30% reduction near the borders of the geometrical acceptance of the muon chambers.

The hadron misidentification probability, measured both in data and in simulation, was cross-checked using pions from K_s^0 and τ decays and compatible results were found. In Analysis I, II and IV the simulated hadrons misidentified as muons were reweighted according to the probability measured in data. In Analysis III a different approach was used to estimate the misidentification probability, as described in Section 8.3, and good agreement with the above results was found.

5.2 Electron identification

Charged particles with momenta greater than 3 GeV/ c and within the efficient acceptance region of the HPC ($0.03 < |\cos \theta_e| < 0.72$) were selected as electron candidates on the basis of the information from the HPC, the TPC and the RICH detectors. Tracks were extrapolated to the HPC and associated to detected showers. The signals from the various detectors were then analyzed by a neural network. By using the network response obtained in a sample of simulated electrons from b and c decays, a momentum dependent cut was defined in order to have a 65% efficiency, constant over the full momentum range.

To reduce the contamination from electrons produced from photon conversions, electron candidates were removed if they came from a secondary vertex and carried no transverse momentum relative to the direction from the primary to this secondary vertex.

The efficiency of tagging an electron was measured in the data by means of a sample of isolated electrons extracted from selected Compton events and a sample of electrons produced from photon conversions in the detector. The ratio between the values of the efficiencies measured in real and simulated events was parameterized in terms of the p_t and the polar angle of the track and found to be on average 0.92 ± 0.02 and 0.93 ± 0.02 , in the 1994 and 1995 samples, respectively. A corresponding correction factor was then applied to the sample of electrons in simulated $q\bar{q}$ events.

The probability of tagging a hadron as an electron was also measured in the data by selecting a background sample by means of the anti b -tag technique in the same manner as for muons. The measured misidentification probability in data and the ratio with the same quantity obtained in simulated events were on average $(0.40 \pm 0.02)\%$ and 0.76 ± 0.05 in the 1994 sample and $(0.38 \pm 0.04)\%$ and 0.70 ± 0.06 in the 1995 sample.

5.3 Simulated lepton sample

Samples of simulated events, which were processed through the same analysis chain as the data as described in Section 3, were used to obtain reference spectra for the different sources of simulated leptons.

The b semileptonic decays to electrons and muons were simulated using the model of Isgur et al. [12] (ISGW model in the following). The model of Bauer et al. [13], which takes into account the finite mass of the produced lepton, was used for the b decays into τ 's. For D decays the branching ratios were adjusted to be in better agreement with measured values [2]. In the different semileptonic decay modes, the branching fractions for the decays to neutral pions, when not measured, were obtained imposing isospin invariance. Reference spectra with alternative models have been obtained reweighting the events according to the decay model considered. The weight was computed on the basis of the lepton momentum in the $B(D)$ rest frame. According to the prescription of [14], for the central value of the results, the inclusive model of Altarelli et al. [15] (ACMM model in the following) was used, with model parameters tuned to the CLEO data [16], whereas ISGW and ISGW** models have been used to evaluate the systematic uncertainties. ISGW** indicates the ISGW model modified to include a 32% contribution of charmed excited states (referred to as D^{**}), instead of the original 11% predicted by the model itself, so as to better describe the CLEO data.

Leptons from the decay chain $b \rightarrow cW \rightarrow c\bar{c}q \rightarrow c\ell^- X$ (the so called “upper decay vertex”) were considered with the contributions from both $D_s \rightarrow \ell^- X$ and $\bar{D}^0(D^-) \rightarrow \ell^- X$.

6 Analysis I: Measurement of semileptonic b decays from single leptons and di-leptons spectra

In this analysis the semileptonic branching fractions for primary and cascade b decays $\text{BR}(b \rightarrow \ell^-)$, $\text{BR}(b \rightarrow c \rightarrow \ell^+)$, $\text{BR}(b \rightarrow \bar{c} \rightarrow \ell^-)$ and the average b mixing parameter, $\bar{\chi}$, are measured using the momentum spectra of single lepton and di-leptons in opposite jets. The single lepton spectra are studied in a sample of events highly enriched in $b\bar{b}$, selected by means of a b -flavour tagging algorithm. In the di-lepton sample, the $b\bar{b}$ purity is increased by requiring a minimum p_t for one of the leptons.

The sensitivity to the different sources of leptons is given by the kinematic properties of leptons from different sources and by the charge correlation between di-leptons in opposite jets from b and \bar{b} , respectively.

Hadronic events and lepton candidates were selected as described in Sections 3 and 5. The angular region $|\cos\theta_{thrust}| < 0.9$ was used for di-lepton candidates, while for single lepton events, to have a good efficiency in the b -flavour tagging, events were considered only if they fulfilled $|\cos\theta_{thrust}| < 0.7$. As a consequence, only barrel muon chambers were considered for single muons. About 768 000 and 385 000 Z hadronic decays were selected in the 1994 and 1995 data samples, respectively.

6.1 Single lepton fit

Events were divided into two hemispheres with respect to a plane perpendicular to the thrust axis and passing through the beam interaction point. A primary vertex was reconstructed in each hemisphere to suppress possible correlations between the two hemispheres induced by the b -tagging algorithm. The combined b -flavour tagging algorithm described

in Section 4 was used to select hemispheres enriched in b -hadron content while, in the opposite hemisphere, the single lepton spectra were studied. For the cut on the combined b -tagging variable used in this analysis, the following efficiencies for selecting different flavours were estimated from simulation: $\varepsilon_b = (39.34 \pm 0.05)\%$, $\varepsilon_c = (1.87 \pm 0.02)\%$, $\varepsilon_{uds} = (0.189 \pm 0.003)\%$, so that the fraction of b events in the sample was $\mathcal{P}_b = 95.1\%$.

The value of ε_b is quoted only for reference, since it is never used in the following. In practice the number N_b^H of tagged hemispheres which contain a b quark was estimated as:

$$N_b^H = N_{tag}^H - (\varepsilon_c \times R_c + \varepsilon_{uds} \times R_{uds}) \times 2N_{had}$$

where: N_{tag}^H and N_{had} are the total numbers of tagged hemispheres and the number of hadronic events, respectively, ε_c and ε_{uds} were the efficiencies for charm and light quark events, respectively, obtained from simulation, and $R_{uds} = \Gamma_{uds}/\Gamma_{had} = 1 - R_b - R_c$. The LEP averages of 0.21643 ± 0.00073 and 0.1694 ± 0.0038 were used for R_b and R_c , respectively [17]. The number of $b\bar{b}$ events used in the simulation was normalized to the same value N_b^H .

Once a hemisphere was tagged as b , leptons were studied in the opposite hemisphere. A correction was applied, estimated from simulation, because of the correlation between the lifetime and the lepton tags. It arose mainly from the acceptance requirements, which are different for electrons and muons, and amounted to $\rho_e = 1.003 \pm 0.005$ and $\rho_\mu = 1.017 \pm 0.005$. Here ρ is the fraction of lepton candidates found in the hemisphere opposite to the b -flavour tagged hemisphere, compared to the fraction of lepton candidates found in an unbiased b hemisphere. Before calculating the lepton transverse momentum, a search for secondary vertices was performed using the same algorithm as in [11]. When the secondary vertex was successfully reconstructed (about 45% of the events), the primary to secondary vertex direction was found to give a better approximation of the b -hadron flight direction than the jet axis, and was used in its place. The resolution on the b -hadron flight direction improved correspondingly from 30 to 20 mrad.

Lepton candidates were classified according to their different origin as follows:

- a) direct b -decay:
 $b \rightarrow \ell^- + X$,
- b) “right sign” cascade decays:
 $b \rightarrow \bar{c} + X \rightarrow \ell^- + X$,
- c) “wrong sign” cascade decays:
 $b \rightarrow c + X \rightarrow \ell^+ + X$,
- d) b decays into τ lepton:
 $b \rightarrow \tau^- + X \rightarrow \ell^- + X$,
- e) direct c -decay
 $c \rightarrow \ell^+ + X$,
- f) prompt leptons from J/Ψ decays or from b or c decays, where the $c\bar{c}$ ($b\bar{b}$) pair is produced by gluon splitting,
- g) misidentified or decaying hadrons.

The above classification was considered both for electrons and muons, separately.

A binned maximum likelihood fit was used to compare the momentum and transverse momentum spectra of electrons and muons in data with the simulation. The full likelihood expression is reported in appendix.

6.2 Di-lepton fit

The single lepton likelihood was multiplied by a likelihood obtained for di-leptons in opposite hemispheres, in order to separate the $b \rightarrow \ell^-$ from the $b \rightarrow c \rightarrow \ell^+$ and the $b \rightarrow \bar{c} \rightarrow \ell^-$ components and to extract the average mixing parameter $\bar{\chi}$. In the di-lepton sample no b -flavour tag was used in order not to introduce any bias in the composition of the b -hadron sample. The b enrichment was obtained by requiring a minimum p_t for one of the two leptons. The full p_t spectrum was considered for the opposite lepton. For a cut at $p_t > 1.2$ GeV/ c , a b purity of about 88% was obtained using simulated events.

Di-lepton events were separated, for both the data and the simulated samples, into six groups depending on whether the two lepton candidates have the same or opposite charge and on which combination of lepton species (ee , $e\mu$, $\mu\mu$) they belonged to. Lepton pairs were used if the two leptons were separated by at least 90° , while lepton pairs coming from the same jet were omitted from the fit to avoid additional systematic uncertainties in the composition of the cascade lepton sample. In each group, simulated events were separated into di-lepton classes, according to the different possible combinations in the two hemispheres of the above mentioned single-lepton classes (a) to (g). To guarantee a reasonable number of events in each bin, the p and p_t of each lepton in the pair were combined to form a single variable, the combined momentum, p_c , defined as in [19]: $p_c = \sqrt{p_t^2 + \frac{p^2}{100}}$. Two-dimensional reference distributions were obtained for the chosen combinations in the variables (p_c^{min}, p_c^{max}) , where p_c^{min} (p_c^{max}) refers to the smaller (larger) combined momentum.

If $B^0 - \bar{B}^0$ mixing is not considered, the main source of di-leptons having opposite charges are direct b -decays: $(b \rightarrow \ell^-)(\bar{b} \rightarrow \ell^+)$. But, in the presence of mixing, a fraction $2\bar{\chi}(1 - \bar{\chi})$ of these di-leptons have the same charge. Same charge di-leptons also arise from events with one direct b -decay and one cascade b -decay: $(b \rightarrow \ell^-)(\bar{b} \rightarrow \bar{c} \rightarrow \ell^-)$. Because of mixing, a fraction $2\bar{\chi}(1 - \bar{\chi})$ of these events will enter the opposite charge class.

The fraction of leptons of class a, b and c were determined by the fit, whereas contributions from lepton classes (d) to (g) were fixed to the values given in Table 3. The detailed expression of the likelihood function, for single lepton and di-lepton, is reported in appendix.

6.3 Results and systematic uncertainties

The results obtained with the 1994 and 1995 samples and their average are shown in Table 1, where the uncertainties are statistical only. About 12% of the single leptons were also included in the di-lepton sample and the statistical uncertainties have been corrected accordingly.

	1994	1995	1994+1995
BR($b \rightarrow \ell^-$)	0.1066 ± 0.0014	0.1081 ± 0.0019	0.1071 ± 0.0011
BR($b \rightarrow c \rightarrow \ell^+$)	0.0822 ± 0.0049	0.0781 ± 0.0064	0.0805 ± 0.0039
BR($b \rightarrow \bar{c} \rightarrow \ell^-$)	0.0144 ± 0.0044	0.0196 ± 0.0056	0.0164 ± 0.0035
$\bar{\chi}$	0.119 ± 0.016	0.138 ± 0.022	0.126 ± 0.013

Table 1: Results of the fit to the 1994 and 1995 lepton samples and their combination. The uncertainties are statistical only.

In Figure 1 single lepton and di-lepton spectra are shown. The simulation spectra have been reweighted according to the result of the fit. The correlation matrix for the statistical uncertainties is shown in Table 2.

	BR($b \rightarrow \ell^-$)	BR($b \rightarrow c \rightarrow \ell^+$)	BR($b \rightarrow \bar{c} \rightarrow \ell^-$)	$\bar{\chi}$
BR($b \rightarrow \ell^-$)	1.00	-0.241	-0.061	0.086
BR($b \rightarrow c \rightarrow \ell^+$)		1.00	-0.797	-0.159
BR($b \rightarrow \bar{c} \rightarrow \ell^-$)			1.00	0.112
$\bar{\chi}$				1.00

Table 2: Correlation matrix of statistical uncertainties in Analysis I.

The following sources of systematic uncertainties have been considered:

- experimental uncertainty related to lepton measurements:
the muon and electron identification efficiencies and the background due to hadron misidentification have been varied considering their measurement uncertainties in the data-simulation comparisons (see Sections 5.1,5.2). To account for effects related to the difference in topology between the test samples used in Sections 5.1,5.2 and the hadronic environment, an additional uncertainty of $\pm 2\%$ has been applied to the efficiencies, as estimated from simulation. As a consequence, the total relative uncertainties assumed on the leptons efficiencies were $\pm 2.5\%$ and $\pm 3\%$ for muons and electrons, respectively. The residual contamination in the electron sample due to converted photons has been varied by $\pm 10\%$.
The angular distribution between di-leptons is well described by simulation, therefore the angular cut of 90° is assumed not to add any systematic uncertainty.
The fit has been performed using for the p_t calculation both the jet direction and the secondary vertex direction. Half the difference between the results has been used as systematic uncertainty.
- experimental uncertainty related to the b -flavour tagging:
efficiencies to tag c and uds quarks have been varied by 9% and 22%, respectively, according to the uncertainties in [11]. The partial decay widths R_b and R_c have been varied according to their measurement uncertainties.
The correction factors for the correlation between the b -tag and the leptons (ρ_e , ρ_μ) have been varied by twice their statistical uncertainties. The dependence on lepton momentum of the correlation has also been studied. Since the b -tag efficiency is higher in presence of high momentum leptons, the lepton spectrum in hemispheres opposite to a b -tagged one is slightly biased towards low momenta. A correction has been estimated with simulation comparing spectra in tagged and non tagged events and the full effect has been assumed as a systematic uncertainty.
The stability of the result as a function of the cut on the b -flavour tagging variable has been checked to be compatible with the corresponding statistical fluctuations.
- modelling uncertainty related to the assumed physical parameters:
the mean value and the range of variation of several physical parameters used in the simulation was calculated according to references [2], [14] and [17]. In particular they have been varied: the mean fractional energy of b and c hadrons, the branching fractions assumed for $b \rightarrow \tau \rightarrow \ell$, $b \rightarrow J/\Psi \rightarrow \ell$, $c \rightarrow \ell$ and the fraction of gluon splitting to heavy quarks. The lepton distribution from the “upper vertex” was studied by varying the contributions of $D_s \rightarrow \ell^- X$ and $\bar{D}^0(D^-) \rightarrow \ell^- X$ of the

DELPHI

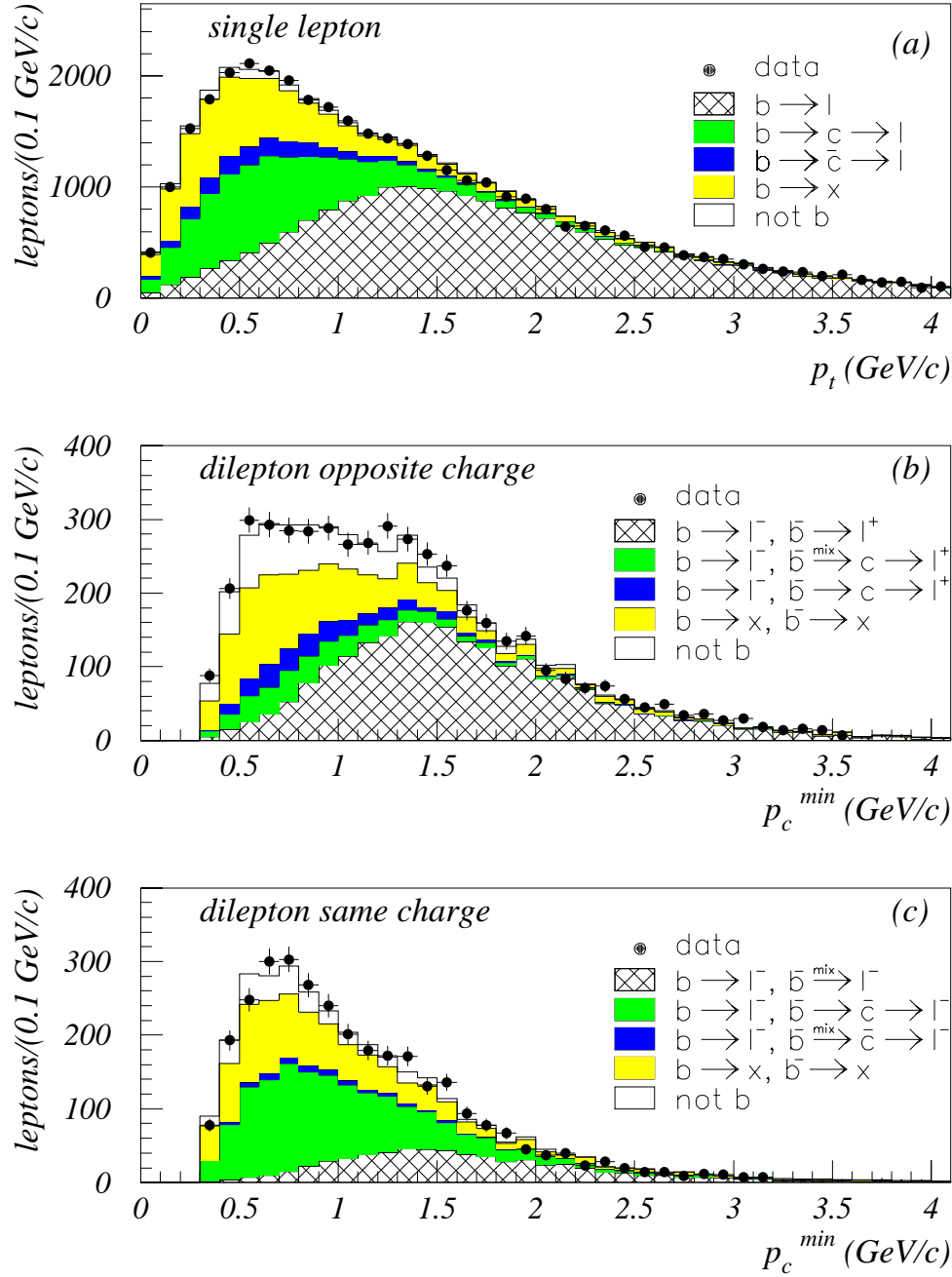


Figure 1: Comparison of data and simulation spectra. The simulation spectra have been reweighted according to the result of the fit. (a) Transverse momentum distribution for single electrons and muons. $b \rightarrow x$ indicates b decays to misidentified or decaying hadrons. (b)((c)) Combined momentum distribution for the two leptons in di-lepton events, identified in opposite jets and having the opposite (same) charge. p_c^{\min} refers to the minimum combined momentum of the two leptons. In the legend of (b) and (c) the lepton origin in the two hemispheres is described, the label “mix” refers to events where $B^0 - \bar{B}^0$ mixing occurred.

Error Source	Range	$\Delta\text{BR}(b \rightarrow \ell^-)$ 10^{-2}	$\Delta\text{BR}(b \rightarrow c \rightarrow \ell^+)$ 10^{-2}	$\Delta\text{BR}(b \rightarrow \bar{c} \rightarrow \ell^-)$ 10^{-2}	$\Delta\bar{\chi}$ 10^{-2}
electron efficiency	$\pm 3\%$	∓ 0.15	∓ 0.14	∓ 0.06	± 0.02
misidentified e	$\pm 8\%$	∓ 0.05	∓ 0.14	∓ 0.06	± 0.04
converted photons	$\pm 10\%$	< 0.01	∓ 0.06	∓ 0.03	± 0.01
μ efficiency	$\pm 2.5\%$	∓ 0.14	∓ 0.18	∓ 0.05	± 0.06
misid. μ barrel, forward	$\pm 6.5\%, 17\%$	∓ 0.01	∓ 0.15	∓ 0.06	± 0.02
jet direction	see text	$+0.05$	-0.03	-0.08	$+0.6$
ε_c	$\pm 9\%$	± 0.02	∓ 0.01	∓ 0.01	± 0.03
ε_{uds}	$\pm 22\%$	± 0.01	± 0.02	< 0.01	∓ 0.02
$\ell - b$ correlation	$\pm 1\%$	∓ 0.05	∓ 0.11	∓ 0.03	± 0.03
$\ell - b$ corr. p dependence	see text	∓ 0.04	± 0.03	∓ 0.01	∓ 0.04
R_b	0.21643 ± 0.00073 [17]	< 0.01	< 0.01	< 0.01	< 0.01
R_c	0.1694 ± 0.0038 [17]	< 0.01	< 0.01	< 0.01	< 0.01
$x_E(b)$	0.702 ± 0.008 [14]	∓ 0.11	± 0.07	± 0.04	∓ 0.15
$x_E(c)$	0.484 ± 0.008 [14]	∓ 0.02	± 0.03	∓ 0.03	± 0.02
$\frac{b \rightarrow W \rightarrow D}{b \rightarrow W \rightarrow D_s}$	$(1.28^{+1.52}_{-0.61})$ [14]	± 0.03	$+0.20$ -0.11	-0.23 $+0.13$	-0.09 $+0.07$
$\text{BR}(b \rightarrow \tau \rightarrow \ell)$	$(0.459 \pm 0.071)\%$ [2]	∓ 0.02	∓ 0.03	∓ 0.04	± 0.02
$\text{BR}(b \rightarrow J/\psi \rightarrow \ell^+ \ell^-)$	$(0.07 \pm 0.01)\%$ [2]	∓ 0.03	± 0.01	± 0.01	∓ 0.09
$\text{BR}(c \rightarrow \ell^+)$	$(9.85 \pm 0.32)\%$ [17]	∓ 0.01	∓ 0.03	∓ 0.04	± 0.01
$g \rightarrow c\bar{c}$	$(3.19 \pm 0.46)\%$ [17]	< 0.01	< 0.01	< 0.01	< 0.01
$g \rightarrow b\bar{b}$	$(0.251 \pm 0.063)\%$ [17]	< 0.01	< 0.01	< 0.01	± 0.01
total systematic		± 0.26	± 0.38	± 0.25	± 0.64
Semilept.mod.b $\rightarrow \ell$ [14]	ACCMM ($+_{\text{ISGW}}$ $-_{\text{ISGW**}}$)	-0.24 $+0.41$	$+0.23$ -0.29	$+0.14$ -0.23	-0.23 $+0.28$
Semilept.mod.c $\rightarrow \ell$ [14]	ACCMM1 ($+_{\text{ACCMM2}}$ $-_{\text{ACCMM3}}$)	-0.08 $+0.07$	-0.11 $+0.01$	-0.03 $+0.02$	-0.33 $+0.34$
total models		-0.25 $+0.42$	$+0.23$ -0.31	$+0.14$ -0.23	-0.40 $+0.44$

Table 3: Summary of systematic uncertainties in the analysis of single and di-lepton events. Ranges given in % correspond to relative variations around the central value.

amount suggested in [14]. Varying the B hadron composition was found to produce negligible effect.

- the modelling uncertainty related to different semileptonic decay models has been calculated according to [14]. Thus the ISGW and ISGW** models have been used as conventional references for evaluating the semileptonic decay model uncertainty and this variation represents the dominant source of systematic uncertainty.
- the finite statistics used in the simulation was checked to introduce a negligible systematic error.

The summary of systematic uncertainties is given in Table 3.

In conclusion from a fit to single and di-lepton events from data collected with the DELPHI detector in 1994 and 1995, the semileptonic branching fractions $\text{BR}(b \rightarrow \ell^-)$, $\text{BR}(b \rightarrow c \rightarrow \ell^+)$, $\text{BR}(b \rightarrow \bar{c} \rightarrow \ell^-)$ and the average b mixing parameter $\bar{\chi}$ have been measured:

$$\begin{aligned} \text{BR}(b \rightarrow \ell^-) &= (10.71 \pm 0.11(\text{stat}) \pm 0.26(\text{syst})_{+0.42}^{-0.25}(\text{model}))\% \\ \text{BR}(b \rightarrow c \rightarrow \ell^+) &= (8.05 \pm 0.39(\text{stat}) \pm 0.38(\text{syst})_{-0.31}^{+0.23}(\text{model}))\% \\ \text{BR}(b \rightarrow \bar{c} \rightarrow \ell^-) &= (1.64 \pm 0.35(\text{stat}) \pm 0.25(\text{syst})_{-0.23}^{+0.14}(\text{model}))\% \\ \bar{\chi} &= 0.126 \pm 0.013(\text{stat}) \pm 0.006(\text{syst}) \pm 0.004(\text{model}) \end{aligned}$$

7 Analysis II: Measurement of semileptonic b decays from single leptons and jet-charge

In this analysis a sample of b enriched events was obtained by applying b -flavour tagging separately to each hemisphere of the event, only events with the thrust axis contained in the region $|\cos\theta_{\text{thrust}}| < 0.8$ were used. The b tagging algorithm exploited only the information from the impact parameters of the tracks from charged particles assigned to the hemisphere: the cut selected 69.2 % of $b\bar{b}$, 12.9 % of $c\bar{c}$ and 1.1 % of uds events, so that the fraction of b events in the sample was $\mathcal{P}_b = 84.0\%$. Leptons were selected from all the charged particles with momentum $p > 3 \text{ GeV}/c$, lying in the hemisphere opposite to the b -tagged hemisphere within the acceptance of the HPC or muon chambers.

The lepton was then used as a seed to reconstruct the position of the b decay vertex, by applying the algorithm originally developed for lifetime and oscillation measurements (for details, see e.g. [20]). A vertex was found in 92.5 ± 0.2 (92.3 ± 0.1)% of the cases in the data (simulation). The direction of the b -hadron was then obtained by averaging the direction of the jet containing the lepton with the one of the vector joining the primary to the secondary vertex: when the vertex was not reconstructed, only the jet direction was used. The energy of the b hadron was computed from the sum of the energy of the charged and neutral particles assigned to its jet and the missing energy in the hemisphere (computed as described in [21]). The resolution was $\sigma(E_B)/E_B \simeq 12\%$. This allowed the entire b -hadron four-momentum to be reconstructed, by assuming an average mass of $\simeq 5.3 \text{ GeV}/c^2$.

Leptons from direct $b \rightarrow \ell^-$ decays were then separated from the other sources of leptons by means of kinematics and charge correlation, as described in the following. The momentum of the lepton in the b -hadron rest frame, k^* , was computed by boosting back the lepton into the b -hadron rest frame: the resolution was about $\sigma_{k^*} \simeq 200 \text{ MeV}/c$. The k^* spectra for $b \rightarrow \ell^-$, $b \rightarrow c \rightarrow \ell^+$, $c \rightarrow \ell^+$ decays in the simulation were tuned as described

in section 5.3 and varied according to the prescriptions already described to compute the systematic uncertainty.

The charge of the lepton, Q_ℓ , was compared to the one of the b jet measured in the opposite hemisphere, Q_b . Neglecting mixing, the product $\lambda_Q = Q_\ell \cdot Q_b$ should be, in case of perfect measurement, $-1/3$ ($+1/3$) for leptons from direct (cascade) decays. The charge of the b quark was determined in each hemisphere by properly combining several quantities (jet charge, vertex charge, charge of any kaon or lepton from b decay, charge of leading fragmentation particles: a detailed description of the method can be found in [22]), such that λ_Q actually ranged between -1 (mostly $b \rightarrow \ell^-$) and $+1$ (mostly $b \rightarrow c \rightarrow \ell^+$). Figure 2 shows the λ_Q distribution for the data and simulation. The fraction of wrong charge assignment, for a given λ_Q range, depends on several quantities related both to the b hadron production and decay mechanisms (B mixing, fragmentation, lepton and K production in b decays, b charged multiplicity, etc.) and to the detector performance (tracking, vertexing, particle identification), which are in some cases not well known. To reduce the systematic uncertainty, the fraction of correct tags was determined in the data, as explained in Section 7.1.

For the previous analysis the charge correlation was only available for the di-lepton sample whereas λ_Q can be determined for all events: it should be noted however that the discrimination power of this variable is smaller. Therefore the two analyses are complementary. Only 1994 data were used for this analysis.

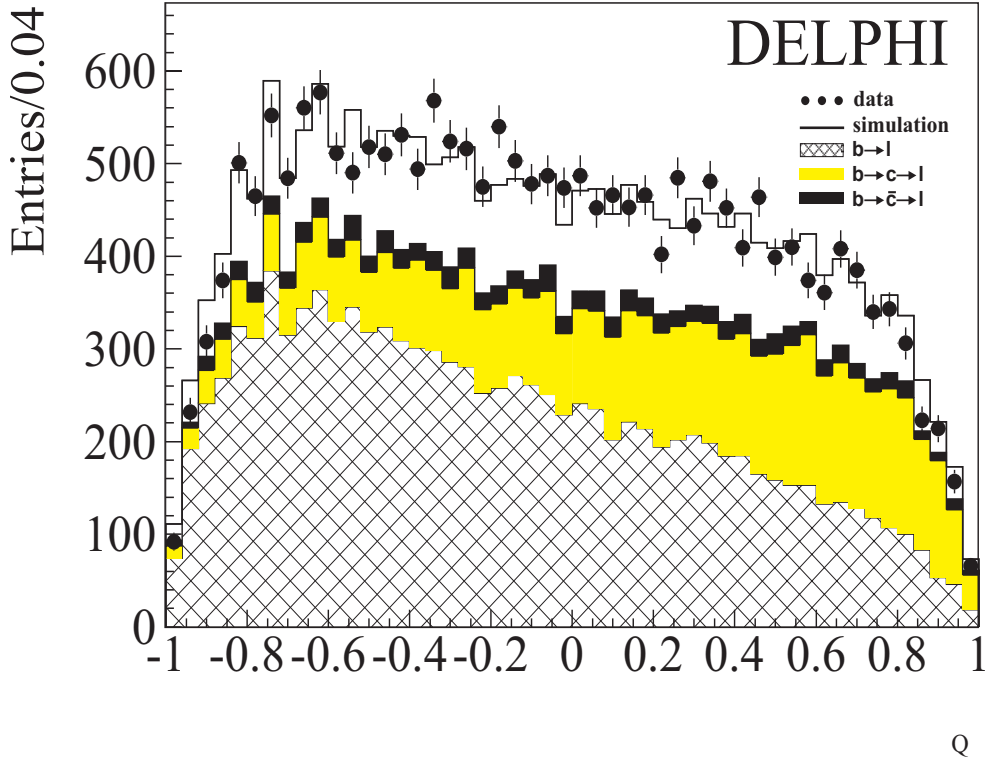


Figure 2: Distribution of the charge correlation variable $\lambda_Q = Q_\ell \cdot Q_b$ for data and simulation.

7.1 Determination of the branching fractions

The b semileptonic branching fractions were obtained by means of a binned χ^2 fit. Leptons in the data and in the simulation were collected in two-dimensional bins, according to their k^* and λ_Q values, so as to exploit fully the discriminating power of the two variables. The k^* bins had adjustable widths, defined such as to correspond to at least 40 entries in each bin. The range of the λ_Q values was divided into an even number (N_{λ_Q}) of bins of the equal width, 4 λ_Q and 25 k^* bins were used.

Events in the simulation were assigned to one of the seven classes described in Section 6.1 depending on their origin. Leptons from classes (d) to (g) were normalized to the data according to the number of hadronic events, known branching ratios and efficiency correction factors. The normalization factors for the classes (a), (b) and (c) were instead determined from the fit and used to compute the branching fractions for the direct ($b \rightarrow \ell^-$) and cascade ($b \rightarrow c \rightarrow \ell^+$, $b \rightarrow \bar{c} \rightarrow \ell^-$) semileptonic decays. Figure 3 shows the fitted k^* distribution in four different λ_Q bins.

The fraction of correct charge tags in each λ_Q bin was determined while performing the fit. For this purpose, the total number of simulated events belonging to the class α ($\alpha=a,b,c$) and falling in the i^{th} (j^{th}) k^* (λ_Q) bin ($\mathcal{N}_{MC}^\alpha(i, j)$) were multiplied by a linear correction factor:

$$\mathcal{N}^\alpha(i, j) = \mathcal{N}_{MC}^\alpha(i, j) \cdot (1 + \delta_j^\alpha)$$

where $\mathcal{N}^\alpha(i, j)$ is the number of data events in the same bin. The δ coefficients would be zero if the simulation described the data perfectly. They were left as free parameters in the fit with the following constraints:

- for a given λ_Q bin, δ does not depend on k^*
- $\delta_j^a = \delta_j^c = \delta_k^b$, where k is the λ_Q bin with opposite charge with respect to j ($k = N_{\lambda_Q} + 1 - j$);
- $\sum_{i,j} \mathcal{N}^\alpha(i, j) = \sum_{i,j} \mathcal{N}_{MC}^\alpha(i, j)$ for every α

The first requirement follows from the fact that the λ_Q value is computed in the hemisphere opposite to the lepton, and is therefore uncorrelated with the value of k^* and with all other lepton decay properties. The second constraint expresses the fact that leptons from direct and cascade decays populate mainly cells that are symmetric with respect to λ_Q . The third constraint ensures that the total number of events is conserved. Values of δ of about -7% and +4% have been obtained for classes (a) and (b,c), respectively. The fit results did not change significantly if the same correction was applied to the simulated leptons of the other classes (d-g).

The procedure was performed separately for muons and electrons: consistent results were found. The χ^2 per degree of freedom was 0.95 for muons and 1.23 for electrons. There was no appreciable difference in the χ^2 when using different models to describe the lepton spectra.

	BR($b \rightarrow \ell^-$)	BR($b \rightarrow c \rightarrow \ell^+$)	BR($b \rightarrow \bar{c} \rightarrow \ell^-$)
BR($b \rightarrow \ell^-$)	1.00	0.017	-0.228
BR($b \rightarrow c \rightarrow \ell^+$)		1.00	-0.928
BR($b \rightarrow \bar{c} \rightarrow \ell^-$)			1.00

Table 4: Correlation matrix of statistical uncertainties in Analysis II.

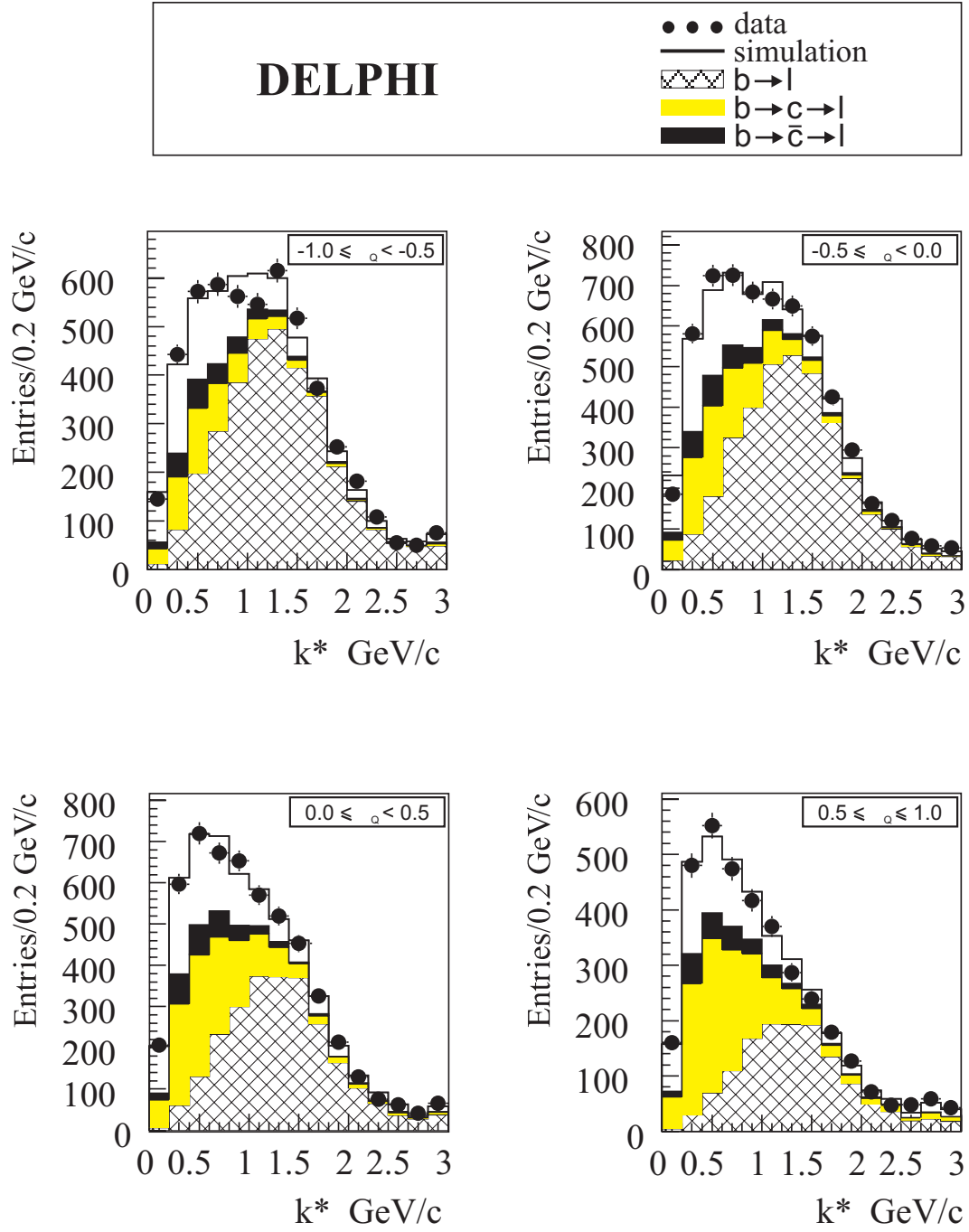


Figure 3: Distribution of the lepton momentum in the b rest frame, k^* , shown in different λ_Q bins.

Error Source	Range	$\Delta\text{BR}(b \rightarrow \ell^-)$ 10^{-2}	$\Delta\text{BR}(b \rightarrow c \rightarrow \ell^+)$ 10^{-2}	$\Delta\text{BR}(b \rightarrow \bar{c} \rightarrow \ell^-)$ 10^{-2}
electron efficiency	$\pm 3\%$	∓ 0.15	∓ 0.12	∓ 0.09
misidentified electrons and converted photons	$\pm 8\%, \pm 10\%$	± 0.01	∓ 0.03	∓ 0.08
μ efficiency	$\pm 2.5\%$	∓ 0.17	∓ 0.09	∓ 0.07
misidentified μ	$\pm 6.5\%$	< 0.01	< 0.01	∓ 0.07
ε_c	$\pm 9\%$	± 0.14	± 0.10	± 0.03
ε_{uds}	$\pm 22\%$	± 0.03	± 0.02	< 0.01
ℓ -btag correlation	$\pm 1\%$	∓ 0.05	∓ 0.11	∓ 0.03
R_b	0.21643 ± 0.00073 [17]	< 0.01	< 0.01	< 0.01
R_c	0.1694 ± 0.0038 [17]	± 0.01	± 0.01	∓ 0.01
binning	± 2 bins	± 0.05	± 0.05	± 0.05
total experimental		± 0.28	± 0.22	± 0.16
$x_E(b)$	0.702 ± 0.008 [14]	< 0.01	< 0.01	< 0.01
$x_E(c)$	0.484 ± 0.008 [14]	∓ 0.02	± 0.02	< 0.01
$\frac{b \rightarrow W \rightarrow D}{b \rightarrow W \rightarrow D_s}$	$(1.28^{+1.52}_{-0.61})$ [14]	± 0.03	$+0.20$ -0.11	-0.23 $+0.13$
$\text{BR}(b \rightarrow \tau \rightarrow \ell)$	$(0.459 \pm 0.071)\%$ [2]	∓ 0.01	∓ 0.04	∓ 0.10
$\text{BR}(b \rightarrow J/\psi \rightarrow \ell^+ \ell^-)$	$(0.07 \pm 0.01)\%$ [2]	∓ 0.02	± 0.01	∓ 0.02
$\text{BR}(c \rightarrow \ell^+)$	$(9.85 \pm 0.32)\%$ [17]	∓ 0.01	< 0.01	∓ 0.02
$g \rightarrow c\bar{c}$	$(3.19 \pm 0.46)\%$ [17]	< 0.01	< 0.01	< 0.01
$g \rightarrow b\bar{b}$	$(0.251 \pm 0.063)\%$ [17]	< 0.01	< 0.01	< 0.01
total systematics		± 0.28	± 0.28	± 0.27
Semilept.mod.b $\rightarrow \ell$ [14]	ACCMM ($+_{\text{ISGW}}$ $-_{\text{ISGW**}}$)	-0.33 $+0.53$	-0.27 $+0.44$	$+0.56$ -0.84
Semilept.mod.c $\rightarrow \ell$ [14]	ACCMM1 ($+_{\text{ACCMM2}}$ $-_{\text{ACCMM3}}$)	-0.08 $+0.06$	-0.22 $+0.09$	$+0.07$ -0.05
total models		-0.34 $+0.53$	-0.35 $+0.50$	$+0.56$ -0.84

Table 5: Summary of systematic uncertainties in the analysis of lepton vs jet charge. Ranges given in % correspond to relative variations around the central value.

The final results, averaged between electrons and muons, are:

$$\begin{aligned} BR(b \rightarrow \ell^-) &= (10.78 \pm 0.14(stat) \pm 0.28(syst)_{+0.53}^{-0.34}(model))\% \\ BR(b \rightarrow c \rightarrow \ell^+) &= (7.59 \pm 0.69(stat) \pm 0.28(syst)_{+0.50}^{-0.35}(model))\% \\ BR(b \rightarrow \bar{c} \rightarrow \ell^-) &= (2.00 \pm 0.49(stat) \pm 0.27(syst)_{-0.84}^{+0.56}(model))\% \end{aligned}$$

The average correlation matrix for the statistical uncertainties is shown in Table 4. The breakdown of the systematic uncertainties for the fit is presented in Table 5. The variation of the k^* resolution causes small differences in the bins population which are included in the binning error.

8 Analysis III: Measurement of semileptonic b decays by applying a multitag method

A measurement of $BR(b \rightarrow \mu)$ and $BR(b \rightarrow c(\bar{c}) \rightarrow \mu)$ using data collected with the DELPHI detector between 1992 and 1995 is presented here. Muons were identified as described in Section 5.1.

In this analysis the contributions of uds , c and b flavours were separated in an inclusive way using a multitag method which used almost all the hadronic events, because it was based on a flavour deconvolution without the need for any further cuts. One important by-product of the method was a systematic and independent analysis of the muon background; as this study cannot be simply applied at electrons due to the presence of photon conversions, all the analysis has been performed with muons only.

The selection of the hadronic events was the same as in Section 3 except that five charged particles instead of seven were required to select the event, and the event thrust axis was required to satisfy $|\cos \theta_{th}| < 0.75$.

The total numbers of selected events both in real and simulated data are shown in Table 6.

8.1 Flavour tagging

The uds , c and b events were separated using the multivariate analysis which was previously applied to the Γ_{bb}/Γ_{had} determination [11]. In each event hemisphere defined with respect to the thrust axis, a set of discriminating variables, called discriminators, were calculated, using lifetime information and event shape variables. These were combined in the *multivariate flavour tagging* algorithm [23] and the *flavour confidence* algorithm [11]. The outputs of these two algorithms were then combined as in [11]. By applying cuts to the combined discriminator and, as in [11], using the enhanced impact parameter tag to define the b-tight category, each hemisphere was classified in one of the following six categories: uds-loose, uds-tight, charm, b-loose, b-standard and b-tight, numbered from 1 to 6 respectively.

The 6 hemisphere categories provide 21 corresponding event categories and hence 21 equations from which the 18-3 independent probabilities, ε_i^j , of classifying a hemisphere of flavour j in category i ($j = b, c, uds$ and $i = 1, \dots, 6$) and the 3-1 independent R_j values, the fractions of flavour j hemispheres in the whole sample, might be determined from a fit to the data. But in practice, because of a rotational ambiguity in the system, 3 additional inputs have to be given. As in [11], these were chosen to be R_c and the probabilities $\varepsilon_{b-tight}^{uds}$ and $\varepsilon_{b-tight}^c$ of classifying charm and uds hemispheres in the b-tight category.

	1992	1993	1994	1995	Total
Simulated	1 369 156	1 232 678	2 275 552	712 868	5 590 254
Real data	486 357	471 437	971 448	467 809	2 397 051

Table 6: Total numbers of selected events for Analysis III

In this analysis the main output of this step is the determination of the probabilities ε_i^j , and hence the flavour content of the different hemisphere categories, rather than that of R_b . The cuts on the combined discriminators have therefore been re-optimized with respect to [11]. The cut on the extended impact parameter tag, however, was kept unchanged in order to keep the values of $\varepsilon_{b-tight}^{uds}$ and $\varepsilon_{b-tight}^c$ unchanged from those determined in [11]. The value of R_b obtained was $R_b = 0.21741 \pm 0.00065$ (stat).

The two main features of this method are the minimal correlation between hemispheres (because the event vertex was computed independently in each hemisphere) and the direct measurement of the tagging efficiencies and of the flavour composition from the data. Since 1994, due to the introduction of double sided silicon detectors measuring z as well as $r\phi$, a better b -flavour tagging has been achieved.

8.2 Flavour deconvolution

The aim of the flavour deconvolution was to extract the spectra of the muon variables p , p_t^{in} and p_t^{out} for each flavour, where p is the momentum of the muon candidate and p_t^{in} and p_t^{out} are its transverse momentum with respect to the jet axis including (p_t^{in}) or excluding (p_t^{out}) the muon in the definition of the jet. Hereafter any of these variables will be referred to as z . The inputs to the flavour deconvolution were the distributions of these variables for each of the six categories defined in the previous section: the category assigned to an identified muon was the category found by the tagging in the opposite hemisphere, in order to avoid correlations between the hemisphere tagging and the presence of the muon.

A χ^2 was then constructed using the number $n_i^\mu(z)$ of identified muons in a given category, i , in an interval of z :

$$\chi^2 = \sum_i \frac{\left(n_i^\mu(z) - N_{hem} \left(\sum_j \varepsilon_i^j R_j D_j^\mu(z) \right) \right)^2}{n_i^\mu(z)} \quad (1)$$

where N_{hem} is the total number of hemispheres, R_j and ε_i^j are the flavour fractions and tagging probabilities extracted from the data as just explained above, and $D_j^\mu(z)$ is the spectrum of the z variable for flavour j extracted from the flavour deconvolution. The above formula neglects correlations between the hemisphere tagging and muon selection efficiencies in opposite hemispheres.

The minimization of this χ^2 function leads to a set of three linear equations for each z bin, where the three unknowns are the components of the spectrum in each flavour: $D_{uds}^\mu(z)$, $D_c^\mu(z)$, $D_b^\mu(z)$. These quantities, and their errors, were computed by solving these equations.

Thus, as a result of the deconvolution, the spectra of identified muons in the different flavours were obtained. They can be written as a function of the different sources of

muons:

$$\begin{aligned}
n_{uds}^\mu(z) &= N_{hem} R_{uds} D_{uds}^\mu(z) = n_{uds}^{bg\mu}(z) \\
n_c^\mu(z) &= N_{hem} R_c D_c^\mu(z) = n_c^{p\mu}(z) + n_c^{bg\mu}(z) \\
n_b^\mu(z) &= N_{hem} R_b D_b^\mu(z) = n_b^{p\mu}(z) + n_b^{bg\mu}(z)
\end{aligned} \tag{2}$$

where $n_{uds}^{bg\mu}(z)$, $n_c^{bg\mu}(z)$ and $n_b^{bg\mu}(z)$ are the distributions of *background* muons for different flavours, and $n_c^{p\mu}(z)$ and $n_b^{p\mu}(z)$ are the distributions of *prompt* muons coming from c and b decays respectively.

This method of flavour deconvolution can also be applied to other kinds of particles and observables. For example, the deconvolution can be applied to all charged particles. The distributions obtained with charged particles are interesting results in themselves, but are here used only to compute the backgrounds $n_c^{bg\mu}(z)$ and $n_b^{bg\mu}(z)$ from $n_{uds}^{bg\mu}(z)$, as described in the next section.

8.3 Background extraction and hadron misidentification probability

In this analysis, a background muon was defined as any particle identified as a muon that either was not a muon, or was a muon but from a light hadron (mainly pion or kaon) decay. Following this definition, all identified muons in uds events were taken as background. The misidentification probability, η_{uds} , was then defined as the fraction of charged particles identified as muons in uds events:

$$\eta_{uds}(z) = \frac{n_{uds}^\mu(z)}{n_{uds}^{tk}(z)} \tag{3}$$

where $n_{uds}^{tk}(z)$ is the spectrum of charged particles with the same kinematic cuts as the muons in the uds sector.

This can be expressed as:

$$\eta_{uds}(z) = \eta^\pi(z) f_{uds}^\pi(z) + \eta^K(z) f_{uds}^K(z) + \eta^\mu(z) f_{uds}^\mu(z) + \eta^o(z) f_{uds}^o(z) \tag{4}$$

where $\eta^\pi(z)$ and $\eta^K(z)$ are the misidentification probabilities for pions and kaons, $f_{uds}^\pi(z)$ and $f_{uds}^K(z)$ are the fractions of pions and kaons for the uds flavour, $f_{uds}^\mu(z)$ is the fraction of muons coming from π and K decays in flight and $\eta^\mu(z)$ is their identification efficiency, and $f_{uds}^o(z)$ and $\eta^o(z)$ are respectively the fraction and the misidentification probability of *other* charged particles, which are mainly protons. The fractions for the different flavours and particles have been measured in DELPHI [24], and agree with the predictions obtained with the JETSET simulation program and used in this analysis. The specific misidentification probabilities ($\eta^\pi(z)$, $\eta^K(z)$, ...) were supposed to be flavour independent but, since the fractions of these particles are not the same in uds , c and b events, a different misidentification probability was evaluated for each flavour (η_{uds} , η_c and η_b). Equation (4) was used to extract $\eta^\pi(z)$, taking $\eta_{uds}(z)$ from the data and $\alpha_{K\pi} = \eta^K(z)/\eta^\pi(z)$, $\eta^\mu(z)$ and $\eta^o(z)$ from the simulation. Then, from equations analogous to (4) written for c and b flavours, η_c and η_b were calculated.

The misidentification probabilities obtained with this method were compared with those obtained using a tight anti- b cut in Section 5.1, and good agreement was observed.

Once the misidentification probability for each flavour was computed, the numbers of background muons per hemisphere for a variable z , i.e. the $n^{bg\mu}(z)$ in (2), were obtained by multiplying them by the number of charged particles per hemisphere for each

flavour. Subtracting these contaminations from the muon candidates per hemisphere, it was possible to determine the distributions of prompt muons.

8.4 Fitting of prompt muon distribution

In order to measure the branching fractions $BR(b \rightarrow \mu)$ and $BR(b \rightarrow c(\bar{c}) \rightarrow \mu)$, the following χ^2 function was then minimized:

$$\chi^2 = \sum_{i=1}^m \frac{\left(n_b^{p\mu}(z_i) - n_b^{p\mu,th}(z_i)\right)^2}{n_b^{p\mu}(z_i)} \quad (5)$$

where m is the number of bins, $n_b^{p\mu}(z_i)$ is the distribution of prompt muons measured as described above, and $n_b^{p\mu,th}(z_i)$ is a model expectation which can be written as:

$$\begin{aligned} n_b^{p\mu,th}(z) &= N_{hem} R_b (1 + BR(g \rightarrow b\bar{b})) \\ &\times [\epsilon_{b \rightarrow \mu}(z) P_{b \rightarrow \mu}(z) BR(b \rightarrow \mu) + \epsilon_{b \rightarrow c(\bar{c}) \rightarrow \mu}(z) P_{b \rightarrow c(\bar{c}) \rightarrow \mu}(z) BR(b \rightarrow c(\bar{c}) \rightarrow \mu)] \\ &+ n_{b \rightarrow \tau \rightarrow \mu}^\mu(z) + n_{b \rightarrow J/\psi \rightarrow \mu}^\mu(z) + n_{g \rightarrow c\bar{c} \rightarrow \mu}^\mu(z) \end{aligned} \quad (6)$$

where $BR(b \rightarrow \mu)$ and $BR(b \rightarrow c(\bar{c}) \rightarrow \mu)$ are the only unknowns, and $P_{b \rightarrow \mu}(z)$ and $P_{b \rightarrow c(\bar{c}) \rightarrow \mu}(z)$ are the true spectra of muons coming from $b \rightarrow \mu$ and $b \rightarrow c(\bar{c}) \rightarrow \mu$ decays which were taken from different models: for the central value, the ACCMM model has been used for $b \rightarrow \mu$ decays and the ACCMM1 model for $c \rightarrow \mu$ decays. The additional terms $n_{b \rightarrow \tau \rightarrow \mu}^\mu(z)$, $n_{b \rightarrow J/\psi \rightarrow \mu}^\mu(z)$ and $n_{g \rightarrow c\bar{c} \rightarrow \mu}^\mu(z)$ are the contributions to *prompt* muons coming from $b \rightarrow \tau \rightarrow \mu$, $b \rightarrow J/\psi \rightarrow \mu$ and $g \rightarrow c\bar{c} \rightarrow \mu$ decays, respectively. The shapes of these distributions have been taken directly from the simulation, but the recommendations of [14] have been followed for their normalizations.

The factors $\epsilon_{b \rightarrow \mu}$ and $\epsilon_{b \rightarrow c(\bar{c}) \rightarrow \mu}$ are global efficiency factors which contain the product of the efficiencies for the momentum cut ($p > 3$ GeV/ c) and the muon geometrical acceptance, evaluated for each of the two considered channels, and the muon identification efficiency.

8.5 Results and systematic errors

The semileptonic branching fractions were obtained minimizing the binned χ^2 of equation (5). In order to check the validity of the method, a test was performed using simulated data. Figure 4 shows a comparison between the muon p_t^{out} distributions at generation level and after deconvolution. A small discrepancy is visible in the b sample. The difference between the generated values of the semileptonic branching fractions and the fit results were found to be 0.8% and 1.4% for the direct and cascade muons, respectively. These differences take into account the approximations used in the analysis. They were used to correct the results obtained with data and were also taken as systematic error contributions.

The results obtained applying the fitting procedure to the real data are shown in Table 7. It can be seen that some variables, which separate the different contributions in different regions, are more discriminant than others. For the transverse momentum, $b \rightarrow c(\bar{c}) \rightarrow \mu$ events are concentrated at low values, while $b \rightarrow \mu$ events are mainly situated at high transverse momentum. On the other hand in the p distribution, in the low momentum region both contributions are of similar importance. Thus the errors on the

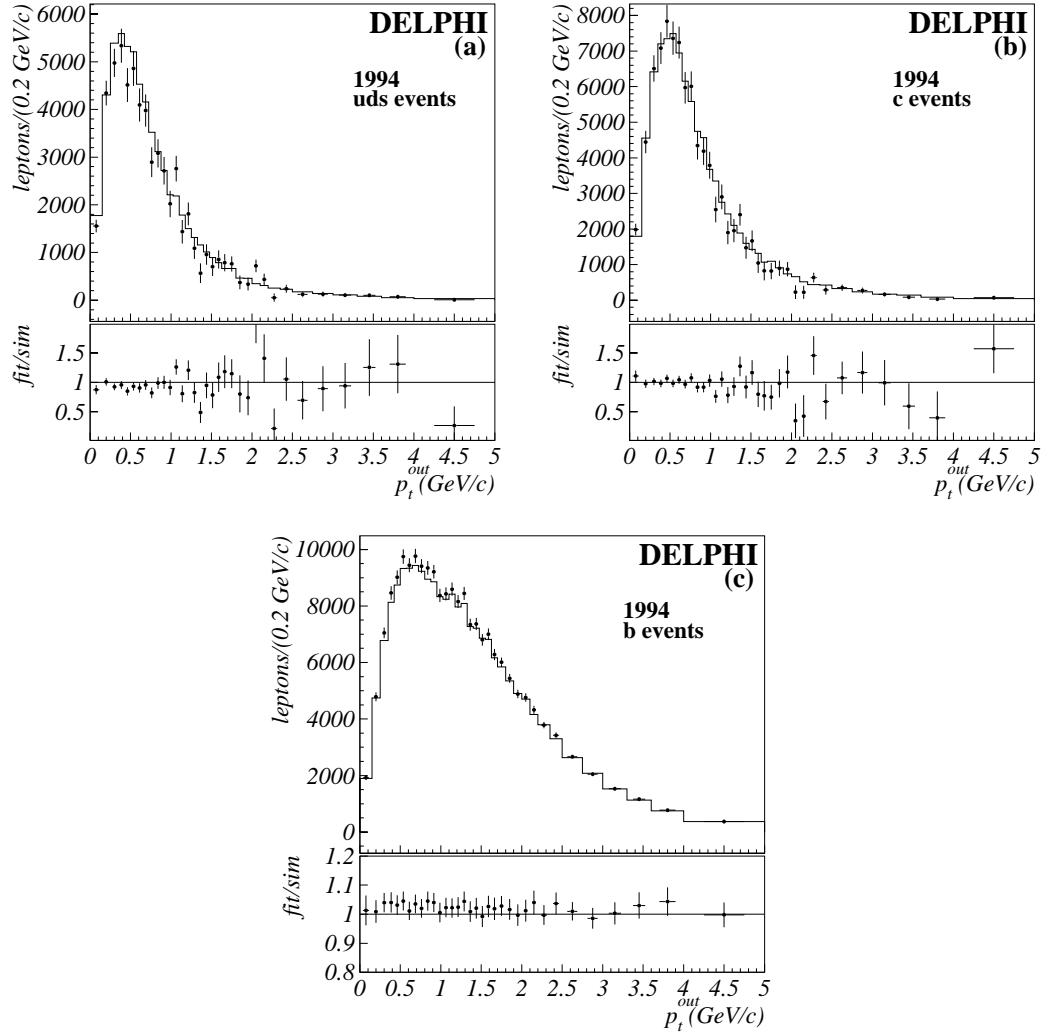


Figure 4: Separation of p_t^{out} spectra of candidate muons between the three flavors. The upper part of each plot compares the results of the deconvolution in simulated data (points) with the generated spectra (solid line); the lower part shows the ratio between these two distributions.

		$b \rightarrow \mu$ (%)	$b \rightarrow c(\bar{c}) \rightarrow \mu$ (%)	χ^2/dof
1992	p	10.78 ± 0.28	9.22 ± 0.46	25.38/27
	p_t^{in}	10.79 ± 0.25	9.68 ± 0.42	25.20/32
	p_t^{out}	10.75 ± 0.22	9.81 ± 0.37	22.75/32
1993	p	10.77 ± 0.29	9.24 ± 0.50	30.62/27
	p_t^{in}	10.68 ± 0.25	9.77 ± 0.45	30.02/32
	p_t^{out}	10.63 ± 0.22	9.78 ± 0.40	41.62/32
1994	p	10.77 ± 0.18	9.60 ± 0.25	43.05/27
	p_t^{in}	10.73 ± 0.16	9.43 ± 0.28	27.74/32
	p_t^{out}	10.62 ± 0.14	9.54 ± 0.24	37.16/32
1995	p	10.76 ± 0.29	9.69 ± 0.45	18.82/27
	p_t^{in}	10.72 ± 0.24	9.86 ± 0.41	24.21/32
	p_t^{out}	10.67 ± 0.21	9.93 ± 0.36	39.26/32

Table 7: Fit result for the real data (the errors are only statistical).

semileptonic branching fractions extracted using the transverse momentum distributions are expected to be lower than those obtained using the momentum distribution.

Once the b semileptonic branching fractions have been fitted, it is possible to calculate the $b \rightarrow \mu$ and the $b \rightarrow c(\bar{c}) \rightarrow \mu$ spectra using the model spectra $P_{b \rightarrow \mu}(z)$ and $P_{b \rightarrow c(\bar{c}) \rightarrow \mu}(z)$. The results are displayed in Figure 5 for each year of data taking. The small contributions coming from the $b \rightarrow \tau \rightarrow \mu$ and $b \rightarrow J/\psi \rightarrow \mu$ decay channels, taken directly from the simulation, are also shown.

Sources of systematic uncertainties have been grouped into several different categories. Here we comment briefly on the features that are specific to this analysis:

- *muon misidentification*: The independent determination of the background distributions in this analysis is affected by
 - the values of f_b^π , f_b^K , f_b^μ and f_b^o which are the fractions of pions, kaons, muons (coming from π and K decays in flight), and other charged particles in b events; the central values were taken from JETSET and the errors (σ) in the table are taken from [24]; 2σ ranges are taken to conservatively cover the degree to which the DELPHI data [24] corroborated the JETSET values.
 - the misidentification probabilities specific to the particles such as η^π , which has been evaluated from η_{uds} , the ratio $\alpha_{K\pi}$, which has been taken from simulation, and η^μ and η^o , whose contribution is small and has also been taken from simulation.
- *hemisphere tagging*: in order to use the multivariate method, three parameters had to be fixed externally: R_c and the probabilities $\varepsilon_{b-tight}^{uds}$ and $\varepsilon_{b-tight}^c$; the variations of the latter probabilities correspond to their systematic uncertainties as evaluated in [11]. The variation corresponding to the difference between the R_b value resulting from this analysis and the reference value used from the other three analyses was found to be negligible.
- *analysis method*: here the effects of different choices made in our analysis are considered, namely (i) the choice of the variable (i.e. p , p_t^{in} or p_t^{out}), (ii) the effect of using a looser muon selection, (iii) the influence of changing the number of bins of our variables, and (iv) the effect of the bias shown in Figure 4 and discussed above.

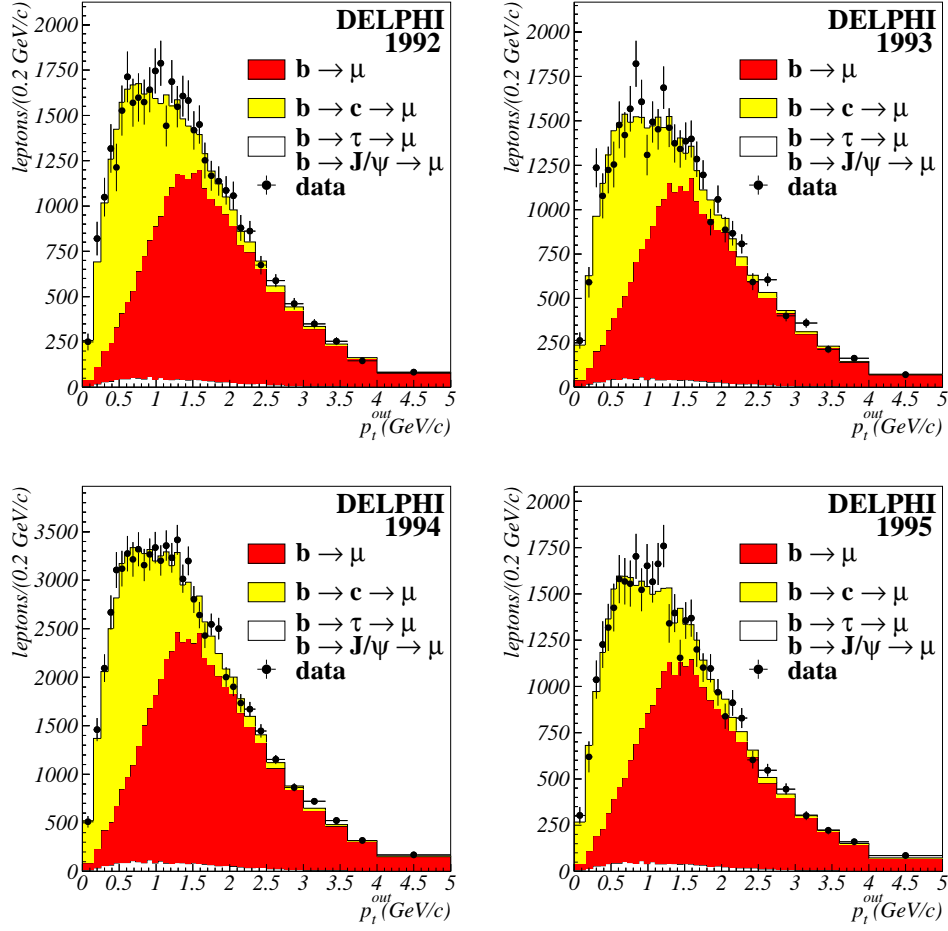


Figure 5: Comparison of the p_t^{out} distributions of prompt muons for the b flavour in real data (dots) with the distributions obtained using the semileptonic branching fractions (histograms). The contributions of different processes are displayed.

For each year the results obtained with the three variables were averaged assuming complete correlation in the statistical error. After averaging over the four years, taking into account the correlations between the systematic errors, the results are:

$$\begin{aligned} BR(b \rightarrow \mu) &= (10.71 \pm 0.11(stat) \pm 0.28(syst)^{-0.37}_{+0.44}(model))\% \\ BR(b \rightarrow c(\bar{c}) \rightarrow \mu) &= (9.62 \pm 0.19(stat) \pm 0.41(syst)^{+0.52}_{-0.49}(model))\% \end{aligned}$$

9 Analysis IV: Measurement of semileptonic b decays from inclusive b -hadron reconstruction and charge correlation

In this analysis the charge correlation between the b quark and the lepton produced in its decay was used to measure the semileptonic decay rates of b -hadrons. The two different cases leading to the like charges, direct decay ($b \rightarrow \ell^-$) and “upper decay vertex” ($b \rightarrow \bar{c} \rightarrow \ell^-$), were separated on the basis of different lepton momentum regions.

To use the charge correlation method, b -hadrons containing a b -quark, H_b , needed to be separated from those containing a \bar{b} -quark, $H_{\bar{b}}$. This separation was accomplished in four steps: 1) by isolating $b\bar{b}$ events, 2) by reconstructing the b -hadron decay vertex, 3) by identifying the tracks from the b -hadron vertex and finally 4) by estimating the hadron charge. The details of these four steps are described below in section 9.1.1 to 9.1.4. After the separation, the sign of the charge of the b -quark and that of the lepton were compared, and each lepton was classified into “like-sign” or “opposite-sign” categories. The fit of the like-sign spectrum was performed assuming the sample was composed of $b \rightarrow \ell^-$ - and $b \rightarrow \bar{c} \rightarrow \ell^-$ -decays, whereas the opposite-sign spectrum assumed only $b \rightarrow c \rightarrow \ell^+$ -decays.

9.1 B reconstruction and separation between H_b and $H_{\bar{b}}$

9.1.1 Event selection

Hadronic events were selected in the same manner as described in Section 3 and the event thrust axis was required to be within the region $|\cos \theta_{thrust}| < 0.75$ to ensure a good b -tagging efficiency. In addition, good detector operating conditions were required for all detectors, including the RICH detector, used for hadron identification. Such requirements led to the selection of 644 792 and 223 082 events in 1994 and 1995 data taking periods, respectively. Each event was then divided into two hemispheres with respect to the thrust axis, and the combined b -tagging algorithm described in Section 4 was applied to select hemispheres enriched in b -hadron content. The number of tagged hemispheres which contain a b quark was estimated using the same technique as in Section 6.1. A slightly different cut on the combined b -tagging variable was used in this analysis, obtaining in simulation the following c and uds efficiencies: $\varepsilon_b = (42.50 \pm 0.06(stat))\%$, $\varepsilon_c = (3.01 \pm 0.02(stat))\%$, $\varepsilon_{uds} = (0.329 \pm 0.003(stat))\%$. This led to the purity of all b -tagged hemisphere being $(92.6 \pm 0.3(stat))\%$.

For each b -tagged hemisphere, lepton candidates were selected in the opposite hemisphere using the same criteria as in Section 5. This method avoids introducing a bias on the relative fraction of the different b -hadron species in the hemispheres where lepton candidates were selected.

9.1.2 Reconstruction of the b -hadron vertex

In reconstructing the b -hadron decay vertex, the rapidity method presented in reference [25] was used. The reference axis for the rapidity calculation was defined by the jet direction obtained using the LUCCLUS algorithm with the transverse momentum as the distance between jets and the parameter d_{join} set to 5 GeV/ c . The rapidity of each charged and neutral particle with respect to the reference axis was calculated, the particles outside the central rapidity window of ± 1.5 were selected as b -hadron decay products and used to reconstruct the secondary vertex. A raw b -hadron mass and energy were computed from the sum of the momentum vectors of the selected particles in the jet. These values were corrected depending on the reconstructed mass and hemisphere energy. This led to a relative energy resolution of about 7% for 75% of the b hadrons which constitute a Gaussian distribution, with the remainder making a tail at higher energies.

9.1.3 Identifying tracks from the b -hadron decay vertex

For each charged particle a probability, P_i , that the particle originated from a b -hadron decay rather than from fragmentation was calculated using a neural network. It took into account the particle rapidity and momentum, its probability to originate from the primary vertex, its probability to originate from the fitted secondary vertex, the flight distance and the energy of the hemisphere. Figure 6(a) shows the comparison between the real data and the simulation.

9.1.4 Classification of H_b and $H_{\bar{b}}$

For each hemisphere, the vertex charge $Q_B = \sum Q_i P_i$ and its uncertainty $\sigma_{Q_B} = \sqrt{\sum P_i(1 - P_i)}$ were calculated by using the probability, P_i , and the charge, Q_i , of each particle. These values, combined with the charge of the identified kaon from b -hadron decay, the jet charge and the charge of the leading fragmentation particle were fed into a neural network to classify a b -hadron into H_b or $H_{\bar{b}}$. The jet charge was defined as: $Q_{jet} = \frac{\sum Q_i \cdot |\vec{p}_i \cdot \vec{t}|^\kappa}{\sum |\vec{p}_i \cdot \vec{t}|^\kappa}$, where \vec{t} is the direction of the thrust axis and \vec{p}_i is the momentum of the track. Using simulation, the weighting exponent κ was tuned to optimize the probability of correctly assigning the charge of b -hadron and was chosen to be 0.6. Figure 6(b) shows the comparison between the real data and the simulation.

9.2 Measurements

9.2.1 Lepton selection

The lepton identification was performed as in Section 5. In addition, the lepton candidate was required to originate from the b -hadron decay vertex by requiring its probability P_i to be larger than 0.5.

For each selected lepton, its momentum k^* , in the b -hadron rest frame, was calculated using the b -hadron four-momentum calculated in Section 9.1.2. Since the average resolution on k^* is 0.1 GeV/ c , the k^* distribution was chosen with a bin width of 0.2 GeV/ c to reduce migration effects.

9.2.2 Fitting and results

The k^* distributions of leptons classified as “like-sign” and “opposite-sign” were compared to the expected spectra from simulation and the branching fractions were extracted

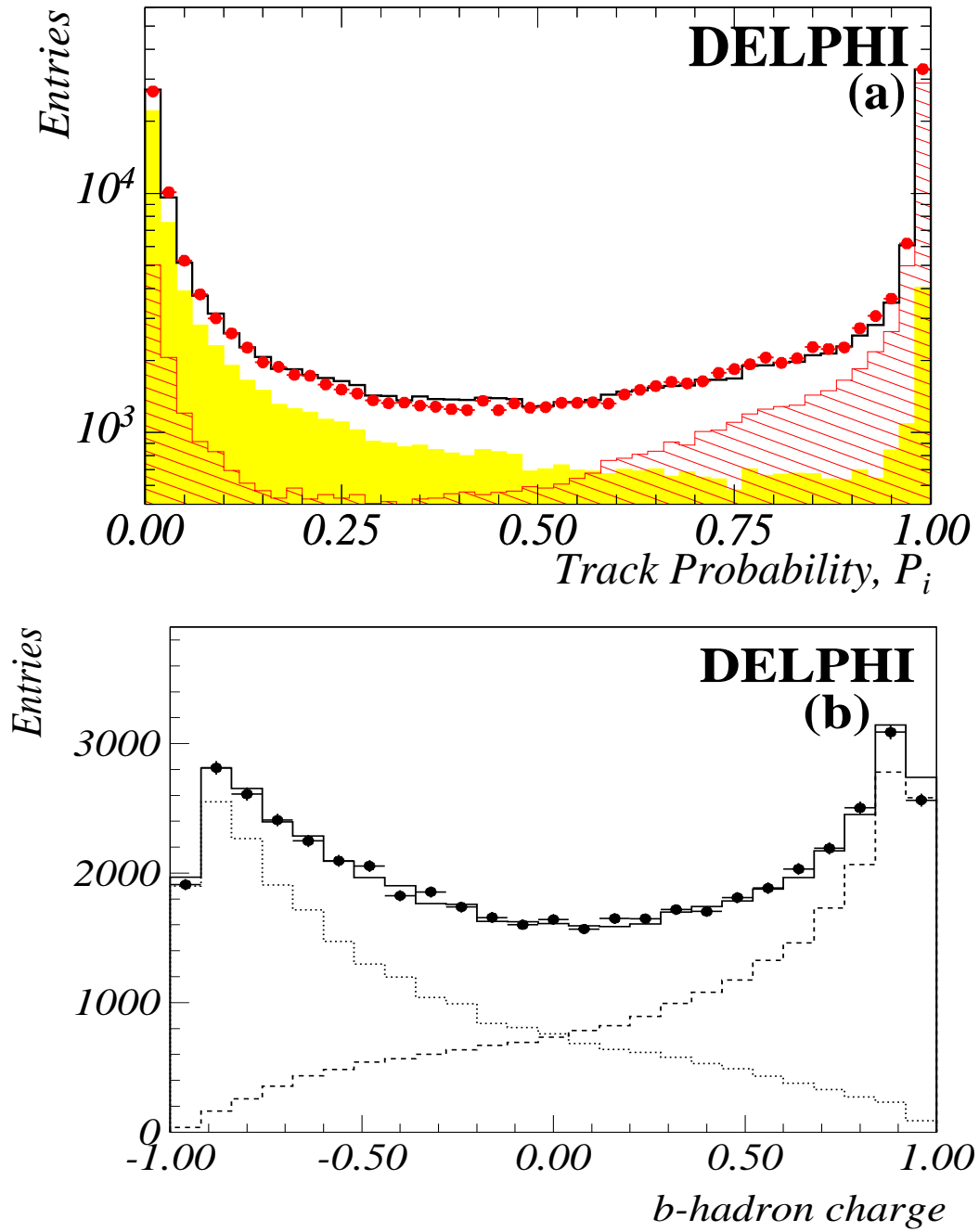


Figure 6: (a) Distribution of the track probability of real data compared to the simulation shown in log scale: Solid (hatched) area represents the tracks from fragmentation (from b -hadron decay). (b) b -hadron charge for real data compared to the simulation: dotted (dashed) curve represents the H_b ($H_{\bar{b}}$).

by means of a χ^2 binned fit. The background contributions which may arise from non- b events, non- b -decay products and wrongly identified leptons were estimated from the simulation and subtracted. Any incorrectly determined charge of the b -quark led to the misclassification of leptons from like-sign to opposite-sign and vice versa. The amount of misclassified leptons was first estimated from the simulation and used in the fit of the lepton spectra. The fraction of each type of decay obtained from the fit was then used to adjust the amount of misclassified leptons. This process was repeated until the fitting results converged.

The following results have been obtained, and Figure 7 shows the results of the fit using the ACCMM model, where the uncertainties are only statistical:

	1994	1995	combined
$\text{BR}(b \rightarrow \ell^-)(\%)$	10.78 ± 0.18	10.67 ± 0.30	10.75 ± 0.15
$\text{BR}(b \rightarrow c \rightarrow \ell^+)(\%)$	8.02 ± 0.31	7.92 ± 0.52	7.99 ± 0.27
$\text{BR}(b \rightarrow \bar{c} \rightarrow \ell^-)(\%)$	1.33 ± 0.32	1.36 ± 0.50	1.34 ± 0.30

The following correlation matrix was found:

	$\text{BR}(b \rightarrow \ell^-)$	$\text{BR}(b \rightarrow c \rightarrow \ell^+)$	$\text{BR}(b \rightarrow \bar{c} \rightarrow \ell^-)$
$\text{BR}(b \rightarrow \ell^-)$	1.00	-0.077	-0.350
$\text{BR}(b \rightarrow c \rightarrow \ell^+)$		1.00	-0.603
$\text{BR}(b \rightarrow \bar{c} \rightarrow \ell^-)$			1.00

9.3 Systematic uncertainties

Since the b reconstruction and the charge evaluation of the b -hadron were done in the hemisphere where the lepton candidate was found, the correlation between the lepton selection and the charge determination of the b hadrons must be studied. Although the lepton information was not included in the training of the neural network to obtain the charge of the b -hadron, a small correlation of $\rho_{bl} = 1.036 \pm 0.005$ was found, where ρ_{bl} represents the ratio of efficiencies to tag a hemisphere which contain a lepton over all hemispheres. This was used to reweight the Monte Carlo events, and twice the statistical error on ρ_{bl} was used to obtain the contribution to the systematic uncertainty.

A more critical bias exists between the neural network output and the b -hadron composition. The neural network output for a hemisphere containing a charged b -hadron was more likely to give the correct charge of the b -quark than a hemisphere containing a neutral b -hadron. The effect of this bias was to increase the likelihood of incorrectly determining the charge of the b -quark for neutral b -hadrons. However, artificially adjusting the Monte Carlo weight to account for this bias resulted in very little change in the branching fractions. A more critical approach was to compare the measured branching fractions with the ones obtained without the charge separation. Without the separation, the lepton spectrum contained the contributions from the direct decay and both modes of the secondary decays. The fit of the three modes was performed by alternatively fixing one rate of the two secondary decays modes, starting with the rate of $b \rightarrow \bar{c} \rightarrow \ell$ fixed to the result of the analysis, until the fit converged. The difference between the branching ratios obtained in this fit and the ones obtained with the charge separation was used as a systematic uncertainty.

The contributions to the systematic uncertainties of the correlation studies are shown in the first part of Table 9. Other sources considered for systematic uncertainties are as follows:

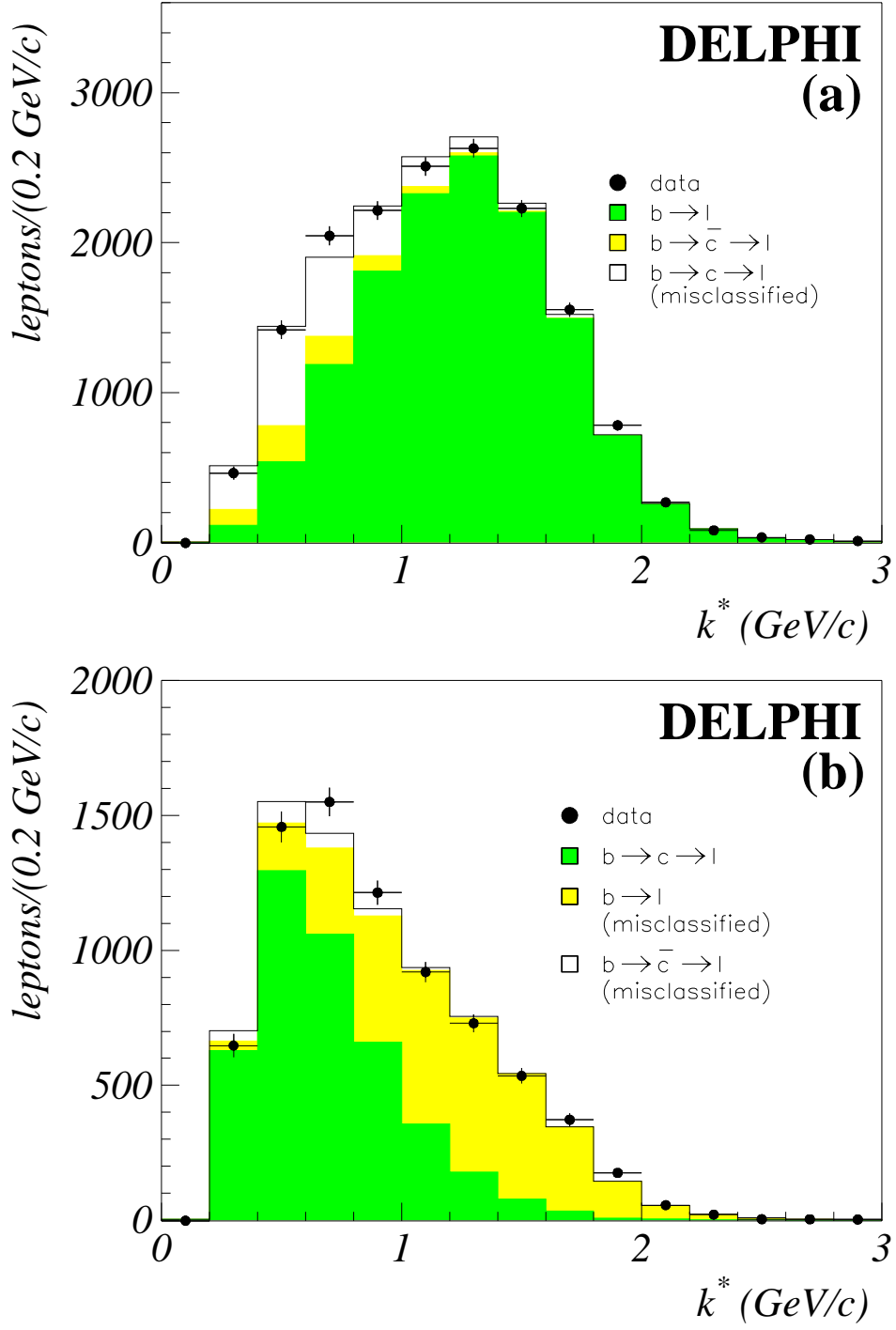


Figure 7: Lepton momentum spectra in the b -hadron rest frame. Plot (a) ((b)) shows the result of the fit with the ACCMM model to the like-sign (opposite-sign) sample .

- **Lepton selection:**
The muon and electron identification efficiencies and the background due to hadron misidentification were varied considering their measurement uncertainties in the data-simulation comparisons (see Sections 5.1, 5.2) as in Analysis I. The residual contamination in the electron sample due to converted photons has been varied by $\pm 10\%$.
- **b -tagging**
The efficiencies to tag c and uds quarks, as well as the values of R_b and R_{uds} , were varied in the same manner as in Analysis I. The correlation between the lifetime tag and the lepton tag was found to be $\rho_e = 1.057 \pm 0.005$ and $\rho_\mu = 1.041 \pm 0.005$. These values were varied by twice their statistical uncertainties.
- **Fitting**
The uncertainty due to the finite Monte Carlo statistics in the lepton spectrum fitting procedure was evaluated.
- **b -hadron composition**
The production fraction for Λ_b was taken from [2] and set to $(10.1^{+3.9}_{-3.1})\%$, and the semileptonic branching fraction was set to $\text{BR}(\Lambda_b \rightarrow \ell \nu X) = (7.4 \pm 1.1)\%$ [26].
- **Models**
The mean fractional energy of c hadrons was varied according to [14].
The lepton distribution from the “upper vertex” was studied by varying the contributions of $D_s \rightarrow \ell^- X$ and $\bar{D}^0(D^-) \rightarrow \ell^- X$ as suggested in reference [14].
The modelling uncertainty related to the branching fractions assumed for $b \rightarrow \tau \rightarrow \ell$, $b \rightarrow J/\Psi \rightarrow \ell$ and to different lepton decay models was also calculated according to [2],[14] and [17].

The summary of the different contributions to systematic uncertainties is given in Table 9. In conclusion, with the method of charge correlation, the following results have been obtained from the data collected with the DELPHI detector in 1994 and 1995:

$$\begin{aligned}
 \text{BR}(b \rightarrow \ell^-) &= (10.75 \pm 0.15(\text{stat}) \pm 0.28(\text{syst})_{+0.43}^{-0.24}(\text{model}))\% \\
 \text{BR}(b \rightarrow c \rightarrow \ell^-) &= (7.99 \pm 0.27(\text{stat}) \pm 0.28(\text{syst})_{+0.10}^{-0.21}(\text{model}))\% \\
 \text{BR}(b \rightarrow \bar{c} \rightarrow \ell^+) &= (1.34 \pm 0.30(\text{stat}) \pm 0.27(\text{syst})_{-0.58}^{+0.36}(\text{model}))\%
 \end{aligned}$$

10 Combinations of results

A comparison of the results obtained in the different analyses described in the previous sections is shown in Table 10. A procedure to combine them in order to produce a final set of physical parameters has been developed. The basic technique, named Best Linear Unbiased Estimator (BLUE) [27], determines the best estimate \hat{x} of a physical parameter built by a linear combination of measurements x_i obtained by several experiments; the coefficients of the combination are built from the covariance matrix E_{ij} of the measured quantities. The method may be easily applied to determine several physical parameters simultaneously, by replacing that matrix with the more general one $E_{i\alpha j\beta}$ where the indices i, j refer to the experiments (here analyses I to IV) and α, β identify the different physical parameters (here $\text{BR}(b \rightarrow \ell^-)$, $\text{BR}(b \rightarrow c \rightarrow \ell^-)$ etc.).

In order to apply this technique, it is necessary to estimate the full error matrix E including the off-diagonal elements; it has been determined as the sum of a statistical part

and a systematic part with the latter accounting for the uncertainties on the parameters used by the analyses and obtained from other measurements.

The statistical part has been built by splitting the statistical error $\sigma_{i\alpha}$ of each parameter α determined by the analysis i into two terms: the first one is computed from the observed number of leptons and is considered as fully correlated between different measurements; the other term is computed in order to keep invariant the total error and is assumed to be uncorrelated.

The estimation of the correlation between the parameters of different analyses is more complicated, as it is necessary to account for the correlation already present inside each single analysis. A reasonable criterion for that is to build the covariance elements by multiplying the correlated parts of the two $\sigma_{i\alpha}$, described above, and by applying a correlation factor determined as an average of the correlation coefficients resulting from the different analyses.

The described procedure can be applied only for identical data samples, while the different analyses used somewhat different data samples; as a consequence the full statistics has been divided into non-overlapping subsamples and the described procedure has been applied to each one of them. To do this the statistical uncertainties on the measurements have been scaled by the ratio of the square root of the number of events used by the corresponding analysis and the square root of the number of events in the subsample itself. These subsamples do not contain any common event and may be assumed uncorrelated; the total covariance matrix may then be obtained by summing the inverse of each covariance matrix and inverting again.

A special care has been put in handling the results of the multivariate analysis which builds up the prompt muon distributions by a linear combination of distributions obtained in 6 categories; the overlap with the b -tagged sample used by the other analyses has been conservatively assumed as corresponding to the category with the biggest purity and therefore the biggest weight.

The systematic part of the error matrix has been evaluated by expressing a linear dependence on the external parameters of each result, and propagating the uncertainties on the parameters themselves; this corresponds to building up the sum of a set of error matrices, one for each uncertainty source, with correlation factors equal to 1 for all pairs of results affected by the corresponding external parameter, while the systematic errors relevant to only some of the results have been added as uncorrelated. The errors arising from the uncertainties on the decay models have not been used in the combination to obtain a result where the dependence on them is most explicit; as these errors give the biggest contribution to the total error this also protects from the instabilities described in the cited paper and in others dealing with this topic [27,28]. The total systematic covariance matrix thus obtained has then been summed to the statistical covariance matrix; the inverse of the sum has been used to weight the four analyses results and find the combined value along with the total error.

The following results have been obtained:

$$\begin{aligned} \text{BR}(b \rightarrow \ell^-) &= (10.70 \pm 0.22)\% \\ \text{BR}(b \rightarrow c \rightarrow \ell^+) &= (7.98 \pm 0.30)\% \\ \text{BR}(b \rightarrow \bar{c} \rightarrow \ell^-) &= (1.61 \pm 0.26)\% \\ \bar{\chi} &= 0.127 \pm 0.014 \end{aligned}$$

where the total error, excluding model effect, is quoted; the global χ^2 of the fit is 1.52 for 12-4=8 degrees of freedom.

The statistical contribution to the total error has been obtained by propagating the statistical uncertainties on the four analyses output to the combined values. The systematic uncertainties breakdown on the combined values have been obtained by combining the error sets given for each analysis, using the same coefficients used to obtain the central values; this is equivalent to observing the effect of changing the combined values by 1σ for each of the error source. The full table of errors is shown in Table 11; the correlation matrix for the statistical and total uncertainties is shown in Table 12.

To investigate the effect of the main assumptions done in this combination (estimation of the correlated part of the error, estimation of the correlation coefficient between different parameters determined in different analyses) the procedure has been repeated after changing them slightly. The off-diagonal element in the error matrix has been changed using the most conservative assumption where a result does not add any information to another one having a smaller uncertainty. Different estimations of the correlation coefficient between different parameters in different analyses have also been tried. Compatible results have been obtained. The combination performed using a covariance matrix built from the statistical errors only was also found to give very similar results.

11 Conclusions

Four different analyses have been used to measure the semileptonic branching fractions for primary and cascade b decays in hadronic Z decays from the data collected by the DELPHI experiment at LEP. Results are compatible and a global average has been obtained:

$$\begin{aligned} \text{BR}(b \rightarrow \ell^-) &= (10.70 \pm 0.08(stat) \pm 0.21(syst)_{+0.44}^{-0.30}(model))\% \\ \text{BR}(b \rightarrow c \rightarrow \ell^+) &= (7.98 \pm 0.22(stat) \pm 0.21(syst)_{-0.20}^{+0.14}(model))\% \\ \text{BR}(b \rightarrow \bar{c} \rightarrow \ell^-) &= (1.61 \pm 0.20(stat) \pm 0.17(syst)_{-0.44}^{+0.30}(model))\% \\ \bar{\chi} &= 0.127 \pm 0.013(stat) \pm 0.005(syst) \pm 0.004(model) \end{aligned}$$

The present result is compatible with and more precise than the previous DELPHI one [5]. It hence supersedes it. It is also compatible with the recent results of the semileptonic branching fraction obtained at LEP [3] and with theoretical calculations [4].

Acknowledgements

We are greatly indebted to our technical collaborators, to the members of the CERN-SL Division for the excellent performance of the LEP collider, and to the funding agencies for their support in building and operating the DELPHI detector.

We acknowledge in particular the support of

Austrian Federal Ministry of Science and Traffics, GZ 616.364/2-III/2a/98,

FNRS-FWO, Belgium,

FINEP, CNPq, CAPES, FUJB and FAPERJ, Brazil,

Czech Ministry of Industry and Trade, GA CR 202/96/0450 and GA AVCR A1010521,

Danish Natural Research Council,

Commission of the European Communities (DG XII),

Direction des Sciences de la Matière, CEA, France,

Bundesministerium für Bildung, Wissenschaft, Forschung und Technologie, Germany,

General Secretariat for Research and Technology, Greece,

National Science Foundation (NWO) and Foundation for Research on Matter (FOM),

The Netherlands,

Norwegian Research Council,

State Committee for Scientific Research, Poland, 2P03B06015, 2P03B1116 and SPUB/P03/178/98,

JNICT-Junta Nacional de Investigação Científica e Tecnológica, Portugal,

Vedecka grantova agentura MS SR, Slovakia, Nr. 95/5195/134,

Ministry of Science and Technology of the Republic of Slovenia,

CICYT, Spain, AEN96-1661 and AEN96-1681,

The Swedish Natural Science Research Council,

Particle Physics and Astronomy Research Council, UK,

Department of Energy, USA, DE-FG02-94ER40817.

References

- [1] *Combined results on b-hadron production rates, lifetimes, oscillations and semileptonic decays*,// LEPHF note 99-02, CERN-EP/00-096.
- [2] Particle Data Group, Eur. Phys. J. **C3** (1998) 1.
- [3] OPAL Collaboration, G. Abbiendi et al., CERN-EP/99-078, submitted to Eur. Phys. J. C;
L3 Collaboration, M. Acciarri et al., Eur. Phys. J. **C 13/1** (1999) 47.
- [4] M. Neubert and C.T. Sachrajda, Nucl. Phys. **B483** (1997) 339.
- [5] DELPHI Collaboration, P. Abreu et al., Z. Phys. **C66** (1995) 323.
- [6] DELPHI Collaboration, P. Aarnio et al., Nucl. Inst. Meth. **A303** (1991) 233;
DELPHI Collaboration, P. Abreu et al., Nucl. Inst. Meth. **A378** (1996) 57.
- [7] N. Binglefors et al., Nucl. Inst. Meth. **A328** (1993) 447;
V. Chabaud et al., Nucl. Inst. Meth. **A368** (1996) 314.
- [8] T. Sjöstrand, CERN-TH/7112/93 (1993), revised August 1995;
Comp. Phys. Comm. **82** (1994) 74.
- [9] DELPHI Collaboration, P. Abreu et al., Zeit. Phys. **C73** (1996) 11.
- [10] JADE Collaboration, W. Bartel et al., Z. Phys. **C33** (1983) 23;
S. Bethke et al., Phys. Lett. **B213** (1988) 235.
- [11] DELPHI Collaboration, P. Abreu et al., Eur. Phys. J. **C10** (1999) 415.
- [12] N.Isgur, D.Scora, B.Grinstein and M.Wise, Phys. Rev. **D39** (1989) 799.
- [13] M. Bauer et al., Z. Phys. **C34** (1987) 103.
- [14] The LEP experiments ALEP, DELPHI, L3 and OPAL, Nucl. Instr. Math. **A378** (1996) 101,
The LEP Electroweak Working Group
Input Parameters for the LEP/SLD Electroweak Heavy Flavor Results LEPHF/98-01, July, 1998 Geneva.
- [15] Altarelli et al., Nucl.Phys. **B208** (1982) 365.
- [16] CLEO Collaboration, S.Henderson et al., Phys. Rev.**D45** (1992) 2212.
- [17] The LEP Collaborations ALEPH, DELPHI, L3, OPAL, the LEP Electroweak Working Group and the SLD Heavy Flavour and Electroweak Groups
A Combination of Preliminary Electroweak Measurements and Constraints on the Standard Model CERN-EP/2000-016, 21 January 2000.
- [18] C. Peterson et al., Phys. Rev. **D 27** (1983) 105.
- [19] P. Acton et al., OPAL Collaboration, Phys. Lett. **B 276**(1992) 379.
- [20] DELPHI Collaboration, P. Abreu et al., Z. Phys. **C 74** (1997) 19.
- [21] DELPHI Collaboration, P. Abreu et al., Z. Phys. **C 71** (1996) 539.
- [22] DELPHI Collaboration, P. Abreu et al., CERN-EP/00-43
Eur. Phys. J. **C 16** (2000) 555.
- [23] P. Billoir et al., Nucl. Inst. Meth. **A360** (1995) 532.
- [24] DELPHI Collaboration, P. Abreu et al., Eur. Phys. J. **C5**(1998) 585.
- [25] DELPHI Collaboration, P. Abreu et al., Z. Phys. **C68** (1995) 353.
- [26] ALEPH Collaboration, R. Barate et al., Eur. Phys. J. **C5** (1998) 205; OPAL Collaboration, R. Akers et al., Z. Phys. **C74** (1997) 423.
- [27] L. Lyons et al., Nucl. Inst. Meth. **A270** (1988) 110-117.
- [28] G. D'Agostini, Nucl. Inst. Meth. **A346** (1994) 306-311.

A Appendix

A.1 Single lepton likelihood

The first part of the likelihood was constructed assuming a Poisson probability, using the single lepton spectra in data and simulation, subdivided in 25×25 bins in the (p_t, p_l) plane. The bins were chosen in such a way to have approximatively the same amount of data in each bins. Nine classes were used, corresponding to the classes (a) to (g) mentioned in section 6.1, with classes (f) and (g) splitted in two, for $b\bar{b}$ and non- $b\bar{b}$ events.

$$\mathcal{L}_1 = \ln(L_1) = \sum_{i=1}^{N_{bin}} \sum_{j=e,\mu} \{ DAT(i, j) \ln(E(i, j)) - E(i, j) \}$$

$$E(i, j) = \sum_{\alpha=1}^{N_{class}} \{ \mathcal{P}(\alpha) MC(i, j, \alpha) \}$$

where $DAT(i, j)$ represent the data and $MC(i, j)$ the simulated spectra, respectively. The $\mathcal{P}(\alpha)$ ($\alpha = 1, 3$) coefficients are the ratio between the unknown branching fractions and the corresponding values used in the simulation:

$$\mathcal{P}(1) = \frac{\text{BR}(b \rightarrow \ell^-)}{\text{BR}(b \rightarrow \ell^-)_{sim}}, \quad \mathcal{P}(2) = \frac{\text{BR}(b \rightarrow c \rightarrow \ell^+)}{\text{BR}(b \rightarrow c \rightarrow \ell^+)_{sim}}, \quad \mathcal{P}(3) = \frac{\text{BR}(b \rightarrow \bar{c} \rightarrow \ell^-)}{\text{BR}(b \rightarrow \bar{c} \rightarrow \ell^-)_{sim}}$$

whereas the \mathcal{P} coefficients corresponding to lepton classes (d) to (g) are fixed to the values given in Table 3.

A.2 Di-lepton likelihood

The second part of the likelihood was constructed assuming a Poissonian probability, using the di-lepton spectra in data and simulation, subdivided in 7×7 bins in the combined momentum variables (p_c^{min}, p_c^{max}) .

The bins were chosen in such a way to have approximatively the same amount of data in each bins. Twenty classes were used, according to the different possible combinations in the two opposite hemispheres of the single-lepton classes (a) to (g) mentioned in section 6.1.

$$\mathcal{L}_2 = \ln(L_2) = \sum_{i=1}^{M_{bin}} \sum_{j=ee,\mu\mu,e\mu} \{ \quad DAT_{same}(i, j) \ln(E_{same}(i, j)) - E_{same}(i, j) +$$

$$\quad DAT_{opp.}(i, j) \ln(E_{opp.}(i, j)) - E_{opp.}(i, j) \}$$

$$E_{same}(i, j) = \sum_{\alpha=1}^{M_{class}} \{ \mathcal{S}(\alpha) MC_{same}(i, j, \alpha) \}$$

$$E_{opp.}(i, j) = \sum_{\alpha=1}^{M_{class}} \{ \mathcal{O}(\alpha) MC_{opp.}(i, j, \alpha) \}$$

where $DAT_{same}(i, j)$ ($DAT_{opp.}(i, j)$) represent the spectra of di-leptons in data, in opposite hemispheres, having the same (opposite) charge and $MC_{same}(i, j)$ ($MC_{opp.}(i, j)$)

represent the simulated spectra. The $\mathcal{S}(\alpha)$ ($\mathcal{O}(\alpha)$) coefficients depend on the ratio between the unknown branching fractions and the corresponding values used in the simulation and on the mixing probability $\bar{\chi}$. For example for the first and the second classes, containing $(b \rightarrow \ell^-, b \rightarrow \ell^-)$ and $(b \rightarrow \ell^-, b \rightarrow c \rightarrow \ell^+)$ di-leptons, respectively:

$$\begin{aligned}\mathcal{S}(1) &= 2\bar{\chi}(1 - \bar{\chi})\mathcal{P}(1)^2 = 2\bar{\chi}(1 - \bar{\chi})\left(\frac{\text{BR}(b \rightarrow \ell^-)}{\text{BR}(b \rightarrow \ell^-)_{sim}}\right)^2 \\ \mathcal{O}(1) &= (1 - 2\bar{\chi}(1 - \bar{\chi}))\mathcal{P}(1)^2 = (1 - 2\bar{\chi}(1 - \bar{\chi}))\left(\frac{\text{BR}(b \rightarrow \ell^-)}{\text{BR}(b \rightarrow \ell^-)_{sim}}\right)^2 \\ \mathcal{S}(2) &= (1 - 2\bar{\chi}(1 - \bar{\chi}))\mathcal{P}(1)\mathcal{P}(2) = (1 - 2\bar{\chi}(1 - \bar{\chi}))\frac{\text{BR}(b \rightarrow \ell^-)\text{BR}(b \rightarrow c \rightarrow \ell^+)}{\text{BR}(b \rightarrow \ell^-)_{sim}\text{BR}(b \rightarrow c \rightarrow \ell^+)_{sim}} \\ \mathcal{O}(2) &= 2\bar{\chi}(1 - \bar{\chi})\mathcal{P}(1)\mathcal{P}(2) = 2\bar{\chi}(1 - \bar{\chi})\frac{\text{BR}(b \rightarrow \ell^-)\text{BR}(b \rightarrow c \rightarrow \ell^+)}{\text{BR}(b \rightarrow \ell^-)_{sim}\text{BR}(b \rightarrow c \rightarrow \ell^+)_{sim}}\end{aligned}$$

The total likelihood is the sum of the single and the di-lepton likelihoods:

$$\mathcal{L} = \mathcal{L}_1 + \mathcal{L}_2$$

In the fit $P(1), P(2), P(3)$ and $\bar{\chi}$ are free parameters, whereas the \mathcal{P} coefficients corresponding to lepton classes (d) to (g) are fixed to the values given in Table 3.

Source	$\Delta(b \rightarrow \mu)$	$\Delta(b \rightarrow c(\bar{c}) \rightarrow \mu)$
muon efficiency ($\pm 2.5\%$)	∓ 0.190	∓ 0.182
$f_b^\pi (\pm 2\sigma)$	∓ 0.004	∓ 0.008
$f_b^K (\pm 2\sigma)$	∓ 0.002	∓ 0.007
$f_b^\mu (\pm 2\sigma)$	± 0.003	± 0.009
$f_b^o (\pm 2\sigma)$	∓ 0.001	∓ 0.001
$\eta^\pi (\pm 2\sigma)$	∓ 0.022	∓ 0.120
$\alpha_{K\pi} (\pm 2\sigma)$	± 0.008	∓ 0.035
$\eta^\mu (\pm 2\sigma)$	∓ 0.004	∓ 0.004
$\eta^o (\pm 2\sigma)$	∓ 0.001	∓ 0.001
$R_b = 0.2170 \pm 0.0009$	< 0.01	< 0.01
$R_c = 0.1734 \pm 0.0048$	< 0.01	< 0.01
$\varepsilon_{b-tight}^{uds} (\pm 15\%)$	± 0.023	± 0.010
$\varepsilon_{b-tight}^c (\pm 7\%)$	± 0.007	± 0.028
Variable	± 0.080	± 0.150
Muon quality	± 0.082	± 0.082
Binning	± 0.078	± 0.079
Bias of the method	± 0.080	± 0.136
MC statistics	± 0.088	± 0.163
$x_E(b) = 0.702 \pm 0.008$	± 0.093	± 0.165
$BR(c \rightarrow \ell) = (9.85 \pm 0.32)\% [17]$	∓ 0.001	∓ 0.002
$BR(b \rightarrow \tau \rightarrow \ell^-) = (0.459 \pm 0.071)\% [2]$	∓ 0.014	∓ 0.096
$BR(b \rightarrow J/\psi \rightarrow \ell^- \ell^+) = (0.07 \pm 0.01)\% [2]$	∓ 0.018	∓ 0.011
$BR(g \rightarrow c\bar{c}) = (3.19 \pm 0.46)\% [17]$	± 0.009	± 0.010
$BR(g \rightarrow b\bar{b}) = (0.251 \pm 0.063)\% [17]$	∓ 0.033	∓ 0.043
total systematic	± 0.28	± 0.41
$b \rightarrow \ell$ $ACCMM_{-ISGW}^{+ISGW}$	-0.35 $+0.43$	$+0.52$ -0.48
$c \rightarrow \ell$ $ACCMM1_{-ACCMM3}^{+ACCMM2}$	-0.11 $+0.11$	-0.12 $+0.02$
total models	$+0.44$ -0.37	$+0.52$ -0.49

Table 8: Analysis III: Systematic uncertainties (%) for $BR(b \rightarrow \mu)$ and $BR(b \rightarrow c(\bar{c}) \rightarrow \mu)$

Source	Range	ΔBR ($b \rightarrow \ell$) $\times 10^{-2}$	ΔBR ($b \rightarrow \bar{c} \rightarrow \ell$) $\times 10^{-2}$	ΔBR ($b \rightarrow c \rightarrow \ell$) $\times 10^{-2}$
ℓ -charge tag correlation	$\pm 1\%$	∓ 0.08	∓ 0.03	∓ 0.09
NN bias on the b -charge	see text	∓ 0.08	∓ 0.15	∓ 0.11
b -hadron composition	see text	∓ 0.04	∓ 0.02	∓ 0.04
electron efficiency	$\pm 3\%$	∓ 0.18	∓ 0.04	∓ 0.15
muon efficiency	$\pm 2.5\%$	∓ 0.13	∓ 0.05	∓ 0.10
Misidentified e	$\pm 8\%$	± 0.01	∓ 0.11	∓ 0.08
Misidentified μ	$\pm 6.5\%$	± 0.01	∓ 0.08	∓ 0.05
Converted γ	$\pm 10\%$	± 0.01	∓ 0.04	∓ 0.03
ε_c	$\pm 9\%$	< 0.01	∓ 0.01	∓ 0.01
ε_{uds}	$\pm 22\%$	< 0.01	± 0.01	∓ 0.01
ℓ - b tag correlation	$\pm 1\%$	∓ 0.09	∓ 0.03	∓ 0.09
R_b	0.21643 ± 0.00073 [17]	< 0.01	< 0.01	< 0.01
R_c	0.1694 ± 0.0038 [17]	< 0.01	< 0.01	< 0.01
MC statistics		∓ 0.03	∓ 0.01	∓ 0.03
$x_E(b)$	0.702 ± 0.008 [14]	± 0.03	± 0.05	± 0.07
$x_E(c)$	0.484 ± 0.008 [14]	∓ 0.01	± 0.01	∓ 0.01
$\frac{b \rightarrow W \rightarrow D}{b \rightarrow W \rightarrow D_s}$	$(1.28^{+1.52}_{-0.61})$ [14]	$^{+0.04}_{-0.04}$	$^{-0.09}_{+0.08}$	$^{+0.03}_{-0.03}$
$\text{BR}(b \rightarrow \tau \rightarrow \ell)$	$(0.459 \pm 0.071)\%$ [2]	∓ 0.02	∓ 0.07	< 0.01
$\text{BR}(b \rightarrow J/\Psi \rightarrow \ell)$	$(0.07 \pm 0.01)\%$ [2]	∓ 0.02	± 0.01	∓ 0.01
$\text{BR}(c \rightarrow \ell)$	$(9.85 \pm 0.32)\%$ [17]	∓ 0.01	∓ 0.05	∓ 0.02
Total systematic		± 0.28	± 0.27	± 0.28
Decay models				
$b \rightarrow \ell$ model	ACCMM ($^{+ISGW}_{-ISGW^{**}}$)	$^{-0.23}_{+0.42}$	$^{+0.36}_{-0.58}$	$^{+0.04}_{-0.04}$
$c \rightarrow \ell$ model	ACCMM1 ($^{+ACCM2}_{-ACCM3}$)	$^{-0.07}_{+0.07}$	$^{+0.06}_{-0.05}$	$^{-0.21}_{+0.09}$
Total Models		$^{-0.24}_{+0.43}$	$^{+0.36}_{-0.58}$	$^{-0.21}_{+0.10}$

Table 9: Analysis IV: Summary of systematic uncertainties. Ranges given in % correspond to relative variations around the central value.

	Analysis I	Analysis II	Analysis III	Analysis IV
$\text{BR}(b \rightarrow \ell^-)\%$	$10.71 \pm 0.11 \pm 0.26$ ^{-0.25 +0.42}	$10.78 \pm 0.14 \pm 0.28$ ^{-0.34 +0.53}	$10.71 \pm 0.11 \pm 0.28$ ^{-0.37 +0.44}	$10.75 \pm 0.15 \pm 0.28$ ^{-0.24 +0.43}
$\text{BR}(b \rightarrow c \rightarrow \ell^+)\%$	$8.05 \pm 0.39 \pm 0.38$ ^{+0.23 -0.31}	$7.59 \pm 0.69 \pm 0.28$ ^{-0.35 +0.50}		$7.99 \pm 0.27 \pm 0.28$ ^{-0.21 +0.10}
$\text{BR}(b \rightarrow \bar{c} \rightarrow \ell^-)\%$	$1.64 \pm 0.35 \pm 0.25$ ^{+0.14 -0.23}	$2.00 \pm 0.49 \pm 0.27$ ^{+0.56 -0.84}		$1.34 \pm 0.30 \pm 0.27$ ^{+0.36 -0.58}
$(\text{BR}(b \rightarrow c \rightarrow \ell^+) + \text{BR}(b \rightarrow \bar{c} \rightarrow \ell^-))\%$	$9.69 \pm 0.24 \pm 0.50$ ^{+0.37 -0.54}	$9.59 \pm 0.30 \pm 0.41$ ^{+0.29 -0.43}	$9.62 \pm 0.19 \pm 0.41$ ^{+0.52 -0.49}	$9.33 \pm 0.26 \pm 0.52$ ^{+0.40 -0.64}

Table 10: Comparison of the results of the different analyses. The measurements are shown using boldface characters, whereas slim-face characters are used for sums which are only shown for comparison. The first uncertainty is statistical, the second is systematic and the third is due to the uncertainty on the semileptonic model.

Error Source	Range	$\Delta\text{BR}(b \rightarrow \ell^-)$ 10^{-2}	$\Delta\text{BR}(b \rightarrow c \rightarrow \ell^+)$ 10^{-2}	$\Delta\text{BR}(b \rightarrow \bar{c} \rightarrow \ell^-)$ 10^{-2}	$\Delta\bar{\chi}$ 10^{-2}
statistical		∓ 0.08	∓ 0.22	∓ 0.20	± 1.3
electron efficiency	$\pm 3\%$	∓ 0.09	∓ 0.08	∓ 0.04	± 0.01
misidentified e	$\pm 8\%$	∓ 0.02	∓ 0.05	∓ 0.03	± 0.04
converted photons	$\pm 10\%$	< 0.01	∓ 0.02	< 0.01	∓ 0.03
μ efficiency	$\pm 2.5\%$	∓ 0.15	∓ 0.12	∓ 0.04	∓ 0.01
misidentified μ	$\pm 6.5\%; 17\%$	< 0.01	∓ 0.03	∓ 0.03	∓ 0.07
ε_c	$\pm 9\%$	± 0.01	± 0.01	± 0.03	± 0.02
ε_{uds}	$\pm 22\%$	± 0.01	< 0.01	< 0.01	< 0.01
$\ell - b$ correlation	$\pm 1\%$	∓ 0.03	∓ 0.05	∓ 0.02	∓ 0.02
other sources		± 0.09	± 0.10	± 0.05	± 0.5
$x_E(b)$	0.702 ± 0.008 [14]	∓ 0.01	± 0.03	± 0.02	± 0.05
$x_E(c)$	0.484 ± 0.008	∓ 0.01	< 0.01	< 0.01	± 0.04
$\frac{b \rightarrow W \rightarrow D}{b \rightarrow W \rightarrow D_s}$	$(1.28^{+1.52}_{-0.61})$ [14]	± 0.02	± 0.08	∓ 0.10	∓ 0.05
$\text{BR}(b \rightarrow \tau \rightarrow \ell)$	$(0.459 \pm 0.071)\%$ [2]	∓ 0.01	∓ 0.02	∓ 0.08	± 0.04
$\text{BR}(b \rightarrow J/\psi \rightarrow \ell^+ \ell^-)$	$(0.07 \pm 0.01)\%$ [2]	∓ 0.02	∓ 0.01	< 0.01	∓ 0.06
$\text{BR}(c \rightarrow \ell)$	$(9.85 \pm 0.32)\%$ [17]	∓ 0.01	< 0.01	∓ 0.02	∓ 0.01
$g \rightarrow c\bar{c}$	$(3.19 \pm 0.46)\%$ [17]	< 0.01	< 0.01	< 0.01	< 0.01
$g \rightarrow b\bar{b}$	$(0.251 \pm 0.063)\%$ [17]	∓ 0.01	∓ 0.01	< 0.01	± 0.01
total systematic		± 0.21	± 0.21	± 0.17	± 0.5
Semilept.mod.b $\rightarrow \ell$ [14]	ACCMM ($^{+}\text{ISGW}$ $^{-}\text{ISGW}^{**}$)	$^{-0.28}$ $^{+0.44}$	$^{+0.10}$ $^{-0.02}$	$^{+0.37}$ $^{-0.47}$	$^{-0.3}$ $^{+0.3}$
Semilept.mod.c $\rightarrow \ell$ [14]	ACCMM1 ($^{+}\text{ACCMM2}$ $^{-}\text{ACCMM3}$)	$^{-0.09}$ $^{+0.08}$	$^{-0.19}$ $^{+0.07}$	$^{+0.05}$ $^{-0.04}$	$^{-0.3}$ $^{+0.3}$

Table 11: Systematic uncertainties associated to the combined results; the effect of sources relevant to only one analysis has been summarized in a single value labelled “other sources”.

	$\text{BR}(b \rightarrow \ell^-)$	$\text{BR}(b \rightarrow c \rightarrow \ell^+)$	$\text{BR}(b \rightarrow \bar{c} \rightarrow \ell^-)$	$\bar{\chi}$
$\text{BR}(b \rightarrow \ell^-)$	1.	-0.066	-0.051	0.018
$\text{BR}(b \rightarrow c \rightarrow \ell^+)$	0.545	1.	-0.733	-0.091
$\text{BR}(b \rightarrow \bar{c} \rightarrow \ell^-)$	0.231	-0.277	1.	0.038
$\bar{\chi}$	0.039	-0.040	0.018	1.

Table 12: Correlation matrix of combined results. On the upper-right side the statistical coefficients are reported, on the lower-left side the statistical+systematic coefficients are shown.